

國立交通大學  
電機與控制工程學系

碩士論文

順滑模態理論應用於有限元素法模式之

撓性臂控制

Sliding Mode Theory Applied to the control  
of FEM-based Flexible Arm

研究生：張人中

指導教授：陳永平 教授

中華民國九十五年六月

順滑模態理論應用於有限元素法模式之  
撓性臂控制

Sliding Mode Theory Applied to the control  
of FEM-based Flexible Arm

研究生：張人中

Student : Jen-Chung Chang

指導教授：陳永平 博士

Advisor : Dr. Yon-Ping Chen

國立交通大學

電機與控制工程學系



A Thesis

Submitted to Department of Electrical and Control Engineering  
College of Electrical and Computer Engineering  
National Chiao Tung University

In Partial Fulfillment of the Requirements  
For the degree of Master

In

Electrical and Control Engineering

June 2006

Hsinchu, Taiwan, Republic of China

中華民國九十五年六月


# 順滑模態理論應用於有限元素法模式之 撓性臂控制

學生：張 人 中

指導教授：陳永平 博士

國立交通大學電機與控制工程學系

## 摘 要



在本篇論文中，我們研究如何穩健控制撓性臂頂端位置的問題。首先以有限元素法推導撓性臂的數學模型，將非線性的撓性臂的高階模式省略，求出一個近似的線性數學模型。而這些被省略的高階撓性臂模式，與系統結構的不確定項一起當成系統外在的擾亂。知名的穩健順滑模式理論可以對付這些擾亂，做有效的控制。模擬以及實驗的結果顯示順滑控制理論的穩健以及在控制結果上的優越。

# Sliding Mode Theory Applied to the control of FEM-based Flexible Arm

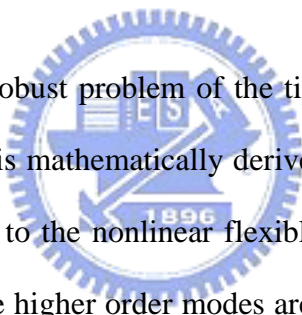
Student: Jen-Chung Chang

Advisor: Dr. Yon-Ping Chen

Department of Electrical and Control Engineering

National Chiao Tung University

## ABSTRACT

The logo of National Chiao Tung University is a circular emblem. It features a gear-like outer border. Inside, there is a stylized representation of a building or structure, with the year '1896' at the bottom. The logo is semi-transparent and overlaid on the abstract text.

This thesis studies the robust problem of the tip position control of a physical flexible arm. Its linear model is mathematically derived by the finite element method (FEM), which is approximate to the nonlinear flexible arm by neglecting the higher order modes. As a result, these higher order modes are considered as the disturbances of the linear model of the flexible arm. In addition, uncertainties subject to the structure and payload variations are also included in the linear model. To cope with these disturbances and uncertainties, the well-known robust control technique, the sliding-mode control, is employed to effectively control the tip position of the flexible arm. Finally, simulation and experimental results are used to demonstrate the robustness and superiority of the sliding mode control.

# Acknowledgement

首先要對指導教授 陳永平教授至上最高的敬意，對於我研究方面的指導與英文寫作表達上的督促，使我這兩年來成長收穫許多。還有可變結構實驗室的桓展，克聰，建峰，豐洲，世宏學長，及宜穎，思穎，仲賢以及學弟妹們在研究所兩年歲月裡的陪伴，無論是研究課業上的分享討論，或是研究之餘的互相鼓勵打氣，都讓我擁有最棒的研究環境和心情。

最後要特別感謝的是我的父母，以及弟弟，感謝你們對我的支持與關心，謝謝你們，沒有你們就沒有這篇論文。

僅以此論文獻給所有關心，照顧我的親朋好友們。

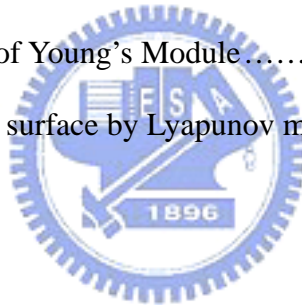


張人中 6.16.2006

# Contents

<b>Chinese Abstract</b> .....	i
<b>English Abstract</b> .....	ii
<b>Acknowledgement</b> .....	iii
<b>Contents</b> .....	iv
<b>List of Figures</b> .....	vi
<b>List of Tables</b> .....	ix
<b>Notations</b> .....	x
<b>Chapter 1 Introduction</b>	
1.1 Preliminary .....	1
1.2 Content Organization.....	2
<b>Chapter 2 System Modeling of a Flexible Arm</b>	
2.1 Introduction .....	3
2.2 FEM-Based Model Description .....	4
2.3 Nature Frequency Analysis of the Flexible Arm .....	12
2.4 Parameter Identification .....	14
<b>Chapter 3 Controller Design</b>	
3.1 Introduction .....	19
3.2 Rigid Controller Design .....	19
3.3 Introduction to the Variable Structure Control (VSC) .....	20
3.4 Sliding Mode Controller Design .....	22
<b>Chapter 4 Simulation Results</b>	
4.1 Pole Placement .....	28
4.2 Sliding Mode Controller Simulation Results .....	30

<b>Chapter 5 Experimental Demonstration</b>	
5.1 Experimental Setup .....	34
5.1.1 Matlab xPC Target Environment .....	34
5.1.2 Motor Setup .....	36
5.1.3 Deflection Measurement .....	37
5.2 Sliding Mode Controller Experimental Results .....	43
5.3 Experimental Results of Impulse Disturbance .....	52
5.4 Experimental Results with Tip-Mass Loading .....	58
<b>Chapter 6 Conclusions</b> .....	66
<b>Reference</b> .....	67
Appendix A   Local mass matrix and stiffness matrix .....	69
Appendix B   Measurement of Young's Module.....	71
Appendix C   Design sliding surface by Lyapunov method.....	74



# List of Figures

Fig. 2.2.1 The flexible arm structure .....	5
Fig. 2.2.2 Four degrees of freedom of an element .....	8
Fig. 2.2.3 Shape functions .....	9
Fig. 2.4.1 Experimental plant .....	14
Fig. 2.4.2 (a) Coupled model frequency response.....	17
Fig. 2.4.2 (b) Uncoupled model frequency response .....	18
Fig. 3.3.1 Sliding Mode Control input combined with different inputs.....	21
Fig. 3.4.1 $Sgn(s)$ function .....	25
Fig. 3.4.2 $Sat(s)$ function .....	26
Fig. 4.1.1 The system poles of the flexible arm .....	29
Fig. 4.1.2 The desired poles of the sliding mode controller.....	30
Fig. 4.2.1 Hub angle regulation in sliding mode control .....	31
Fig. 4.2.2 Four states response in sliding mode control .....	31
Fig. 4.2.3 Sliding surface in sliding mode control .....	32
Fig. 4.2.4 Norm of the error states in sliding mode control .....	32
Fig. 4.2.5 Tip position regulation in sliding mode control .....	33
Fig. 5.1.1 Hardware Architecture .....	35
Fig.5.1.2 Wheatstone Bridge Circuit .....	38
Fig.5.1.3 Voltage Amplifier Circuit .....	39
Fig.5.1.4 Low Pass Filter Circuit .....	40
Fig.5.1.5 Low Pass Filter Bode Plot .....	40
Fig. 5.2.1 Hub angle regulation in rigid control .....	44
Fig. 5.2.2 Tip position regulation in rigid control .....	45



Fig. 5.2.3 Four states response in rigid control .....	45
Fig. 5.2.4 Hub angle regulation in SMC ( $\varepsilon = 0.01$ and $\sigma = 5$ ).....	46
Fig. 5.2.5 Tip position regulation in SMC ( $\varepsilon = 0.01$ and $\sigma = 5$ ).....	46
Fig. 5.2.6 Four states response in SMC ( $\varepsilon = 0.01$ and $\sigma = 5$ ) .....	47
Fig. 5.2.7 Sliding surface in SMC ( $\varepsilon = 0.01$ and $\sigma = 5$ ) .....	47
Fig. 5.2.8 Hub angle regulation in SMC ( $\varepsilon = 0.0067$ and $\sigma = 6$ ).....	48
Fig. 5.2.9 Tip position regulation in SMC ( $\varepsilon = 0.0067$ and $\sigma = 6$ ) .....	48
Fig. 5.2.10 Four states response in SMC ( $\varepsilon = 0.0067$ and $\sigma = 6$ ) .....	49
Fig. 5.2.11 Sliding surface in SMC ( $\varepsilon = 0.0067$ and $\sigma = 6$ ) .....	49
Fig. 5.2.12 Hub angle regulation in SMC ( $\varepsilon = 0.005$ and $\sigma = 8$ ) .....	50
Fig. 5.2.13 Tip position regulation in SMC ( $\varepsilon = 0.005$ and $\sigma = 8$ ) .....	50
Fig. 5.2.14 Four states response in SMC ( $\varepsilon = 0.005$ and $\sigma = 8$ ) .....	51
Fig. 5.2.15 Sliding surface in SMC ( $\varepsilon = 0.005$ and $\sigma = 8$ ) .....	51
Fig. 5.3.1 Hub angle response in rigid control .....	53
Fig. 5.3.2 Tip position response in rigid control .....	54
Fig. 5.3.3 Four states response in rigid control .....	54
Fig. 5.3.4 Frequency response of vibration in rigid control .....	55
Fig. 5.3.5 Hub angle response in sliding mode control .....	56
Fig. 5.3.6 Tip position response in sliding mode control .....	56

Fig. 5.3.7 Four states response in sliding mode control .....	57
Fig. 5.3.8 Sliding surface in sliding mode control .....	57
Fig. 5.3.9 Frequency response of vibration in sliding mode control .....	58
Fig. 5.4.1 Hub angle regulation in rigid control ( $m_t = 0.102\text{kg}$ ) .....	59
Fig. 5.4.2 Tip position regulation in rigid control ( $m_t = 0.102\text{kg}$ ) .....	60
Fig. 5.4.3 Four states response in rigid control ( $m_t = 0.102\text{kg}$ ) .....	60
Fig. 5.4.4 Hub angle in SMC ( $m_t = 0.102\text{kg}$ , $\varepsilon = 0.01$ and $\sigma = 6$ ) .....	61
Fig. 5.4.5 Tip position in SMC ( $m_t = 0.102\text{kg}$ , $\varepsilon = 0.01$ and $\sigma = 6$ ) .....	61
Fig. 5.4.6 Four states response in SMC ( $m_t = 0.102\text{kg}$ , $\varepsilon = 0.01$ and $\sigma = 6$ ) ....	62
Fig. 5.4.7 Sliding surface in SMC ( $m_t = 0.102\text{kg}$ , $\varepsilon = 0.01$ and $\sigma = 6$ ) .....	62
Fig. 5.4.8 Hub angle in SMC ( $m_t = 0.102\text{kg}$ , $\varepsilon = 0.005$ and $\sigma = 7$ ) .....	63
Fig. 5.4.5 Tip position in SMC ( $m_t = 0.102\text{kg}$ , $\varepsilon = 0.005$ and $\sigma = 7$ ) .....	63
Fig. 5.4.6 Four states response in SMC ( $m_t = 0.102\text{kg}$ , $\varepsilon = 0.005$ and $\sigma = 7$ ) .	64
Fig. 5.4.7 Sliding surface in SMC ( $m_t = 0.102\text{kg}$ , $\varepsilon = 0.005$ and $\sigma = 7$ ) .....	64

# List of Tables

Table 2.4.1: Physical parameters of the system .....	15
Table 2.4.2: Nature frequencies (Hz) of coupled and uncoupled models .....	17
Table 5.1.2 Servo Motor Specifications .....	36



# Notations

$\mathbf{A}, \mathbf{B}, \mathbf{C}$  : Upper-case bold italic letters denote matrices.

$\mathbf{a}, \mathbf{b}, \mathbf{c}$  : Lower-case bold italic letters denote vectors.

$a, b, c$  : Lower-case italic letters denote scalars.

$w$  : Deformation of beam.

$\theta$  : Rotary angle of hub.

$\rho$  : mass per unit length.

$E$  : Young's modulus of elasticity.

$I$  : area moment of inertia of the arm's cross section.

$J_h$  : Rotary inertia of hub.

$u$  : Input torque.

$\phi(\cdot)$  : Shape function for beam.

$s$  : Sliding surface.

$sgn(\cdot)$  : The sign function.

$sat(\cdot)$  : The saturation function.

$\varepsilon$  : Width of saturation function.

# Chapter 1

## Introduction

### 1.1 Preliminary

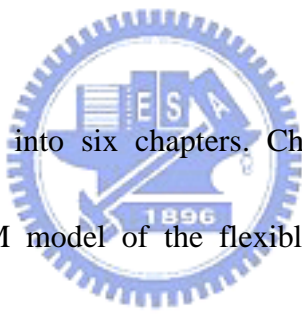
Recently, the control problems of flexible systems have been intensively studied due to the challenging demand of fast and precise manipulators in various industrial and space applications. In future space applications, the manipulators will need to be lighter and to move faster with higher accuracy. The reduced inertias of these lighter and faster manipulators unavoidably result in vibration. Thus, it is important to investigate the dynamics and control problems for manipulators with structure flexibility. The desired control strategy for the flexible arms is not only to control the motion of the rigid mode with reasonable accuracy, but also to suppress the vibration of the arm to achieve high speed and precise tip position.

Since the tip position motion of the lightweight flexible arm has an infinite number of modes, most of the investigators [1, 2, 14, 18] adopt the so-called finite freedom model to simulate the real flexible arm. Instead, this thesis uses the finite element method (FEM) to derive a reduced-order model for the flexible arm.

It is well known that the sliding mode control is an established robust method of

controlling uncertain systems [3]. Besides, the sliding mode control for flexible arms has been widely studied [2, 16, 17, 18]. In these papers, numerical simulation results show that the flexible arm is effectively controlled by SMC. In this thesis, an experimental flexible arm is set up to control the flexible arm tip position. In addition, the robustness of the proposed sliding mode controller is compared with the rigid controller by applying impulse disturbance and payload variation to the flexible arm.

## 1.2 Content Organization



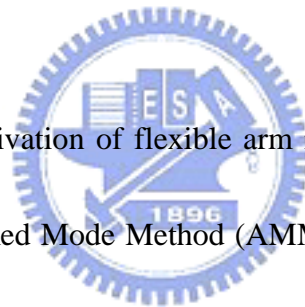
This thesis is organized into six chapters. Chapter 1 gives an introduction. Chapter 2 describes the FEM model of the flexible arm. Chapter 3 presents the scheme and theorem of sliding mode controller. The control purpose in this thesis is to regulate the hub angle of the flexible arm with vibration suppressed. Chapter 4 simulates the flexible arm control in Matlab and then Chapter 5 fulfills the experiment. Finally, concluding remarks are stated in Chapter 6.

# Chapter 2

## System Modeling of a Flexible Arm

Although there are some documents using system identification method to identify the flexible arm model [19], the derived mathematical model is used in this thesis because of its accuracy of physical meaning to describe the nonlinear model.

### 2.1 Introduction



Mathematical model derivation of flexible arm is generally concluded into two methods. One is using Assumed Mode Method (AMM), and the other is using Finite Element Method (FEM). In Assumed Mode Method, the vibration modes in flexible arm are considered as shape functions, and the amplitude of these modes are state variables. The shape function of AMM is more complicated and could not be used for different complex geometry shape system. It means that different plant needs different shape function. FEM divides the flexible arm into several elements, and the shape function of each one is the same. The shape functions are simple polynomial equations and do not change when different complex geometry shape flexible arm is applied. The state variables of FEM model are deformations of all elements which are

easier to get from the strain gauge feedbacks. The FEM-based flexible arm model is derived as follows.

A clamped-free single flexible arm is generally modeled by a partial differential equation [9], expressed as

$$\frac{\partial^2}{\partial x^2} \left( EI \frac{\partial^2 w}{\partial x^2} \right) + \rho \frac{\partial^2 w}{\partial t^2} = p \quad (2.1.1)$$

where

$E$  : Young's modulus of elasticity.

$I$  : area moment of inertia of the arm's cross section.

$w$  : transverse displacement (deformation).

$\rho$  : mass per unit length.

$p$  : external force per unit length.

There is no exact solution for (2.1.1). Instead, an approximate approach using polynomials is adopted to solve the partial differential equation. A more correct solution will be obtained when higher order polynomials are used. FEM is employed to derive the single flexible arm model in this paper.

## 2.2 FEM-Based Model description

The flexible arm is a one-meter stainless steel ruler shown in Fig. 2.2.1. The left-hand side of the arm is clamped on the motor joint and the right-hand side is free. Consider vibration and rotation in horizontal direction and neglect shear deformation, as in the Euler-Bernoulli beam shown in Fig. 2.2.1. The motor rotational angle  $\theta(t)$  and deformation, transverse displacement,  $w(x,t)$  are expressed in the fixed X-Y



coordinate system and reference x-y coordinate system, respectively. To model the FEM structure, it is required that the transverse displacement  $w(x,t)$  be small, less than one tenth of the full arm length.

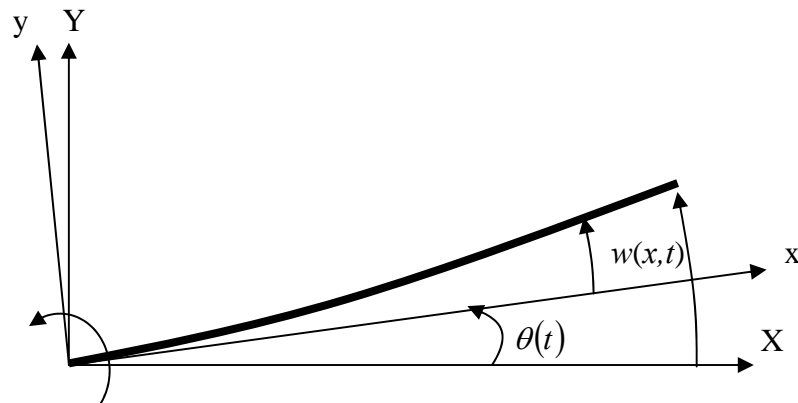
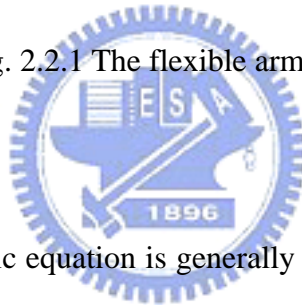


Fig. 2.2.1 The flexible arm structure



The flexible arm dynamic equation is generally derived by Hamilton's principle

described as

$$\int_{t_1}^{t_2} \delta(T - V)dt + \int_{t_1}^{t_2} \delta W_{nc} dt = 0 \quad (2.2.1)$$

where

$T$  : system kinetic energy

$V$  : system potential energy

$\delta W_{nc}$  : virtual work by non-conservative forces

The system kinetic energy is composed of rotational and moving energies, written as

$$T = \frac{1}{2} J_h \dot{\theta}(t)^2 + \frac{1}{2} \int_0^L \rho v(x,t)^2 dx \quad (2.2.2)$$

where  $J_h$  is the rotational inertia of the hub, and

$$v = v(x,t) = \dot{w}(x,t) + (x+r)\dot{\theta}(t)$$

represents flexible arm velocity.

Because the flexible arm rotates on the horizontal plane, the gravity potential energy is neglected, and total system potential energy only contains strain energy, expressed by

$$V = \frac{1}{2} \int_0^L EI \left( \frac{\partial^2 w}{\partial x^2} \right)^2 dx \quad (2.2.3)$$

Virtual work  $\delta W_{nc}$  done by non-conservative force is described as

$$\delta W_{nc} = u_1 \delta \theta(t) \quad (2.2.4)$$

where  $u_1$  is the motor torque applied to the system. Substituting  $T$ ,  $V$  and  $\delta W_{nc}$  into (2.2.1) yields

$$\int_{t_1}^{t_2} \left[ \int_0^L \rho (\dot{w} + (x+r)\dot{\theta}) (\delta \dot{w} + (x+r)\delta \dot{\theta}) dx - \int_0^L EI \left( \frac{\partial^2 w}{\partial x^2} \right) \delta \left( \frac{\partial^2 w}{\partial x^2} \right) dx + J_h \dot{\theta} \delta \dot{\theta} + u_1 \delta \theta \right] dt = 0 \quad (2.2.5)$$

From the truth of

$$\int_{t_1}^{t_2} \frac{\partial T}{\partial \dot{q}_i} \delta \dot{q}_i dt = \frac{\partial T}{\partial \dot{q}_i} \delta q_i \Big|_{t_1}^{t_2} - \int_{t_1}^{t_2} \frac{d}{dt} \left( \frac{\partial T}{\partial \dot{q}_i} \right) \delta q_i dt \quad (2.2.6)$$

and the assumption of  $\delta q_i(t_1) = \delta q_i(t_2) = 0$  in Hamilton's principle, we have

$$\int_{t_1}^{t_2} \frac{\partial T}{\partial \dot{q}_i} \delta \dot{q}_i dt = - \int_{t_1}^{t_2} \frac{d}{dt} \left( \frac{\partial T}{\partial \dot{q}_i} \right) \delta q_i dt$$

and rearrange (2.2.5) as

$$\int_{t_1}^{t_2} \left\{ \int_0^L \left[ \rho(\ddot{w} + (x+r)\ddot{\theta})\delta w + EI \left( \frac{\partial^2 w}{\partial x^2} \right) \delta \left( \frac{\partial^2 w}{\partial x^2} \right) \right] dx + \left[ \int_0^L \rho(x+r)(\dot{w} + (x+r)\dot{\theta}) dx + J_h \ddot{\theta} - u_1 \right] \delta \theta \right\} dt = 0 \quad (2.2.7)$$

where  $w(x,t)$  is the deformation that refers to the rotational reference coordinate system x-y and is described by FEM. Since  $dx$  and  $\delta\theta$  are linear independent, we have

$$\int_0^L \left[ \rho(\ddot{w} + (x+r)\ddot{\theta})\delta w + EI \left( \frac{\partial^2 w}{\partial x^2} \right) \delta \left( \frac{\partial^2 w}{\partial x^2} \right) \right] dx = 0 \quad (2.2.8)$$

$$\left[ \int_0^L \rho(x+r)(\dot{w} + (x+r)\dot{\theta}) dx + J_h \ddot{\theta} - u_1 \right] \delta \theta = 0 \quad (2.2.9)$$

Based on FEM, the flexible arm consists of many linear piecewise arm elements, each with four degrees of freedom (DOF). The deformation  $w(x,t)$  of the  $j$ -th element is written as

$$w(x,t) = \sum_{i=1}^4 \phi_i(x-x_j) v_{ij}(t) \quad x_j < x < x_{j+1} \quad (2.2.10)$$

where  $v_{1j}(t)$  and  $v_{2j}(t)$  ( $v_{3j}(t)$  and  $v_{4j}(t)$ ) represent the transverse deflection and rotation at node  $j$  ( $j+1$ ) as depicted in Fig. 2.2.2, and  $\phi_i(x)$  means the shape functions [6]. To solve the shape functions  $\phi_i(x)$ ,  $i=1,2,3,4$ , the following boundary conditions must

be satisfied

$$\begin{aligned} w(x_j, t) &= v_{1j}(t) \\ \frac{\partial}{\partial t} w(x_j, t) &= v_{2j}(t) \\ w(x_{j+1}, t) &= v_{3j}(t) \\ \frac{\partial}{\partial t} w(x_{j+1}, t) &= v_{4j}(t) \end{aligned} \quad (2.2.11)$$

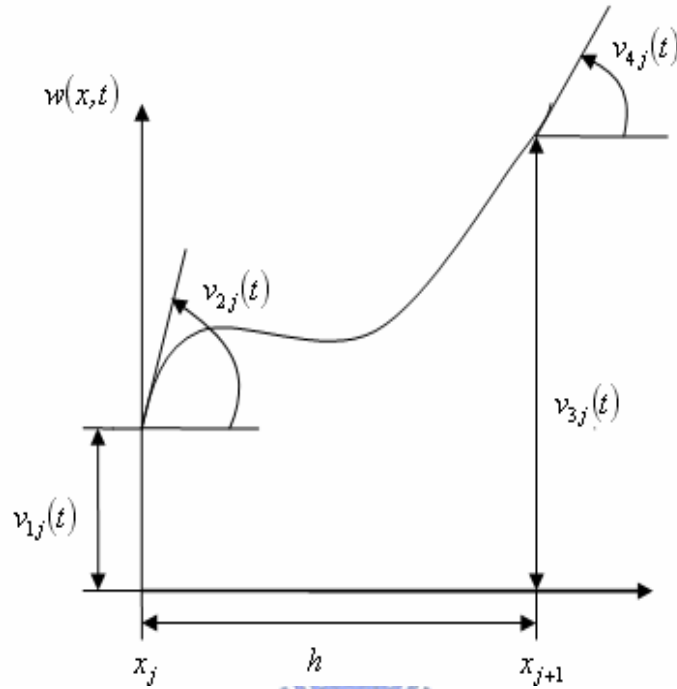


Fig. 2.2.2 Four degrees of freedom of an element



Substituting (2.2.11) into (2.2.10) yields

$$\begin{aligned}
 \phi_1(0) &= 1, \quad \dot{\phi}_1(0) = \phi_1(h) = \dot{\phi}_1(h) = 0 \\
 \dot{\phi}_2(0) &= 1, \quad \phi_2(0) = \phi_2(h) = \dot{\phi}_2(h) = 0 \\
 \phi_3(h) &= 1, \quad \phi_3(0) = \dot{\phi}_3(0) = \dot{\phi}_3(h) = 0 \\
 \dot{\phi}_4(h) &= 1, \quad \phi_4(0) = \dot{\phi}_4(0) = \phi_4(h) = 0
 \end{aligned} \tag{2.2.12}$$

where  $h$  is the length of the flexible arm. Since there are four boundary conditions per interpolation function, the simplest functions we can select are linear polynomials of the form

$$\phi_i(x) = C_{1i} + C_{2i}x + C_{3i}x^2 + C_{4i}x^3, \quad i = 1, 2, 3, 4 \tag{2.2.13}$$

Substitute (2.2.12) into (2.2.13) to solve the four shape functions, which are obtained

as

$$\begin{aligned}
 \varphi_1(x) &= 1 - 3\left(\frac{x-x_j}{h}\right)^2 + 2\left(\frac{x-x_j}{h}\right)^3 \\
 \varphi_2(x) &= (x-x_j) - 2h\left(\frac{x-x_j}{h}\right)^2 + h\left(\frac{x-x_j}{h}\right)^3 \\
 \varphi_3(x) &= 3\left(\frac{x-x_j}{h}\right)^2 - 2\left(\frac{x-x_j}{h}\right)^3 \\
 \varphi_4(x) &= -h\left(\frac{x-x_j}{h}\right)^2 + h\left(\frac{x-x_j}{h}\right)^3
 \end{aligned}
 \quad x_j < x < x_{j+1} \quad (2.2.14)$$

where  $x$  is the distance to the base.

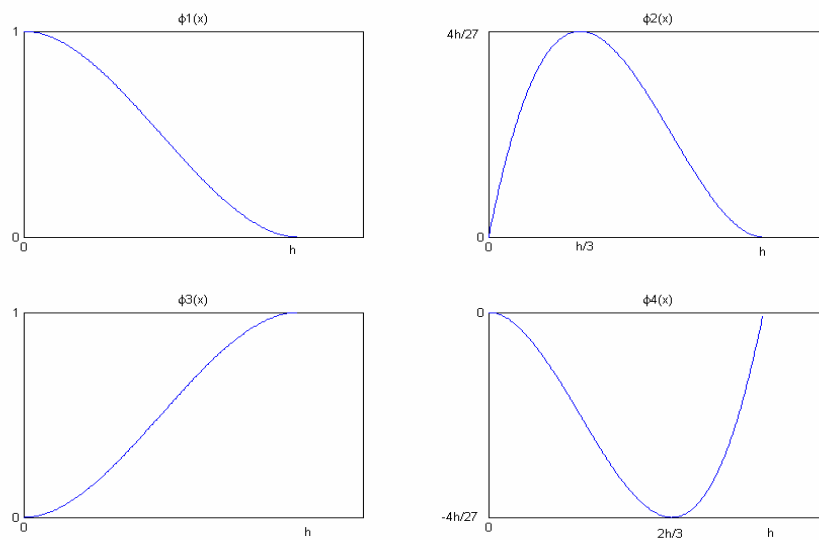


Fig. 2.2.3 Shape functions

Calculate the second partial derivative of  $w(x, t)$  to time and the second partial derivative of  $w(x, t)$  to  $x$ , then

$$\ddot{w}(x, t) = \sum_{i=1}^4 \phi_i(x) \ddot{v}_{ij}(t) \quad (2.2.15)$$

$$\frac{\partial^2 w(x,t)}{\partial x^2} = \sum_{i=1}^4 \frac{\partial^2}{\partial x^2} [\phi_i(x)] v_{ij}(t) \quad (2.2.16)$$

Substituting (2.2.15) and (2.2.16) into (2.2.8) and (2.2.9) and integrating spatial domains leads to the global mass and stiffness matrices (the local mass and stiffness matrices are showed in Appendix A). The assembled set of matrix differential equations is as follows [1, 2, 14, 18]:

$$\mathbf{M} \ddot{\mathbf{x}} + \mathbf{K} \mathbf{x} = \mathbf{b}_N u \quad (2.2.17)$$

where

$N$  is the number of elements,

$$\mathbf{x} = \begin{bmatrix} \theta \\ \mathbf{v} \end{bmatrix}$$

where

$$\mathbf{v} = [v_1 \quad v_2 \quad \cdots \quad v_{2N-1} \quad v_{2N}]^T$$



represents the state variables,

$\mathbf{b}_N = \begin{bmatrix} 1 \\ \mathbf{0} \end{bmatrix}$  represents the single input, and

$\mathbf{M} = \begin{bmatrix} J_h + M_{\theta\theta} & M_{\theta v} \\ M_{v\theta} & M_{vv} \end{bmatrix}$  represents the mass matrix for the FEM-based model.

$\mathbf{K} = \begin{bmatrix} \mathbf{0} & \mathbf{0} \\ \mathbf{0} & \mathbf{K}_{vv} \end{bmatrix}$  represents the stiffness matrix for the FEM-based model.

where

$$M_{\theta\theta} = \sum_{i=1}^N \mathbf{M}_{11}^i$$

$$M_{\theta v} = M_{v\theta}^T = [M_{13}^1 + M_{12}^2 \quad M_{13}^2 + M_{12}^3 \quad M_{13}^3 + M_{12}^4 \quad \cdots \quad M_{13}^{N-1} + M_{12}^{N-1} \quad M_{13}^N]$$



Finally, the tip position defined as [8]

$$\mathbf{t}(\mathbf{x}, \mathbf{t}) = L\theta(\mathbf{t}) + \mathbf{w}(\mathbf{x}, \mathbf{t})$$

is also an important index in this thesis.

### 2.3 Nature frequencies of the flexible arm

To determine the nature frequencies of the flexible arm described in (2.2.17), the inertial matrix  $\mathbf{M}$  is often changed into  $\mathbf{M}_U$  by neglecting the coupling elements between hub coordinate  $\theta$  and flexible coordinates such that the dynamic equation becomes as

$$\mathbf{M}_U \ddot{\mathbf{x}} + \mathbf{K} \mathbf{x} = \mathbf{b}_N \mathbf{u} \quad (2.3.1)$$

where  $\mathbf{M}_U = \begin{bmatrix} J_h + M_{\theta\theta} & \mathbf{0} \\ \mathbf{0} & \mathbf{M}_{VV} \end{bmatrix}$  denotes the uncoupled inertial matrix. Hence, (2.3.1)

can be further decomposed into the following equations

$$(J_h + M_{\theta\theta})\ddot{\theta} = u \quad (2.3.2)$$

$$\mathbf{M}_{VV}\ddot{\mathbf{v}} + \mathbf{K}_{VV}\mathbf{v} = 0 \quad (2.3.3)$$

Furthermore, the matrices  $\mathbf{M}_{VV}$  and  $\mathbf{K}_{VV}$  are symmetric and positive-definite.

$$\mathbf{M}_{VV} = \mathbf{U}^T \mathbf{A} \mathbf{U} = \mathbf{U}^T \mathbf{A}^{\frac{1}{2}} \mathbf{A}^{\frac{1}{2}} \mathbf{U} = \left( \mathbf{A}^{\frac{1}{2}} \mathbf{U} \right)^T \left( \mathbf{A}^{\frac{1}{2}} \mathbf{U} \right) = \mathbf{N}^T \mathbf{N} \quad (2.3.4)$$

where  $\mathbf{U}$  is the orthogonal matrix,  $\mathbf{A}$  is the diagonal matrix, and  $\mathbf{N} = \mathbf{A}^{\frac{1}{2}} \mathbf{U}$ . With



(2.3.4), rewrite (2.3.3) into

$$N\ddot{\mathbf{v}} + \mathbf{K}_{VN}N\mathbf{v} = 0 \quad (2.3.5)$$

where  $\mathbf{K}_{VN} = N^{-T}\mathbf{K}_{VV}N^{-1}$ . It can be found that

$$\mathbf{x}^T\mathbf{K}_{VN}\mathbf{x} = \mathbf{x}^TN^{-T}\mathbf{K}_{VV}N^{-1}\mathbf{x} = (N^{-1}\mathbf{x})^T\mathbf{K}_{VV}(N^{-1}\mathbf{x}) = \mathbf{y}^T\mathbf{K}_{VV}\mathbf{y} \quad (2.3.6)$$

Which implies  $\mathbf{K}_{VN}$  is symmetric and positive definite, same as  $\mathbf{K}_{VV}$ . Hence, it can be written as

$$\mathbf{K}_{VN} = \mathbf{P}^T\mathbf{\Omega}\mathbf{P} \quad (2.3.7)$$

where  $\mathbf{P}$  is the orthogonal matrix and  $\mathbf{\Omega}$  is the diagonal matrix. Substituting (2.3.7)

into (2.3.5) yields

$$N\ddot{\mathbf{v}} + \mathbf{P}^T\mathbf{\Omega}\mathbf{P}N\mathbf{v} = \mathbf{0} \quad (2.3.8)$$

$$\mathbf{P}N\ddot{\mathbf{v}} + \mathbf{\Omega}\mathbf{P}N\mathbf{v} = \mathbf{0}$$



Define a new modified state vector

$$\mathbf{y} = \mathbf{P}N\mathbf{v}, \quad (2.3.9)$$

where  $\mathbf{y}$  is the  $2n \times 1$  vector of model coordinates. The transformed equation of

motion (2.3.3) becomes

$$\ddot{\mathbf{y}} + \mathbf{\Omega}\mathbf{y} = \mathbf{0} \quad (2.3.10)$$

$$\text{where } \mathbf{\Omega} = \begin{bmatrix} \lambda_1 & 0 & \cdots & 0 \\ 0 & \lambda_2 & 0 & 0 \\ \vdots & 0 & \ddots & \vdots \\ 0 & 0 & \cdots & \lambda_{2n} \end{bmatrix} = \begin{bmatrix} w_1^2 & 0 & \cdots & 0 \\ 0 & w_2^2 & 0 & 0 \\ \vdots & 0 & \ddots & \vdots \\ 0 & 0 & \cdots & w_{2n}^2 \end{bmatrix} \quad (2.3.11)$$

where  $w_1, w_2, \dots, w_{2n}$  are the flexible arm frequencies.

## 2.4 Parameter Identification

In order to test and validate the controller designed in this thesis, an experimental setup, which is shown in Fig. 2.4.1, was developed.



Fig. 2.4.1 Experimental plant

The main characteristics of the prototype of Fig. 2.4.1 are shown in Table 2.4.1.

Table 2.4.1: Physical parameters of the system

Arm length $l$	0.94[m]
Arm width	0.031[m]
Arm thick	0.0015[m]
Arm mass $m$	0.3706[kg]
Flexible arm mass per unit length $\rho$	0.3554[kg/m]
Young's modulus $E$	$2.08 \times 10^{11}$ [Nt/m <sup>2</sup> ]
Cross-section inertia momentum $I$	$8.718 \times 10^{-12}$ [m <sup>4</sup> ]
Hub rotary inertia $J_h$	$1.12 \times 10^{-4}$ [kg m <sup>2</sup> ]
Hub radius $r$	0.0265[m]

In Section 2.3, the nature frequencies of the flexible arm, shown in (2.3.12), are derived for its uncoupled model. The Young's modulus  $E$  could be determined from the expression of nature frequencies of the uncoupled model (shown in Appendix B) [17], which is constructed with the flexible arm fixed in the hub. To attain the nature frequencies, an impulse force is generally required as the excitation source. In this experiment, the impulse force is created by a hammer knocking near the root of the flexible arm. After a knock, the strain gage feedback signal of the uncoupled flexible arm is recorded. In order to get the nature frequencies of the uncoupled flexible arm, a Fast Fourier transform (FFT) is performed for the signal to get the primary nature frequencies which results in high amplitude response at the frequencies. For the precise position of the nature frequencies, it is necessary to obtain many samples from many experiments. Using the precise nature frequencies position, the Young's

modulus  $E$  is derived in Appendix B. Since the Young's modulus  $E$  is acquired, the precise nature frequencies of the coupled model can be derived in the same way like the derivation of section 2.3. The difference of the coupled model and the uncoupled model is that the latter is neglecting the coupling elements between hub coordinate  $\theta$  and flexible coordinates. Because the controller is designed for the flexible arm FEM model, it is important to make sure the accuracy of the FEM model. It is a good way to check the accuracy of the FEM model by checking the nature frequencies of the derived FEM model is the same as the experiment flexible arm. So, let the flexible arm free with the hub and give a knock to the arm, the nature frequency response of the coupled model is obtained by performing FFT to the strain gages feedback signal. Finally, compare the nature frequencies of the coupled experimental model with the derived model, the result, Table 2.4.2, shows that they were remarkably close to each other, and it means that the finite-element-method is valid to describe the flexible arm [9].

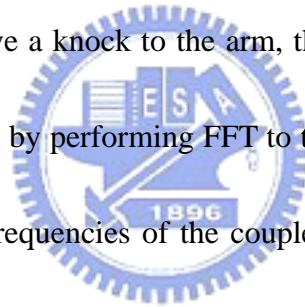


Table 2.4.2: Nature frequencies (Hz) of coupled and uncoupled models

Nature freq.	Coupled Model				Uncoupled model			
	Exp <sup>a</sup>	FEM <sup>b</sup>			Exp	FEM		
		N=2	N=10	N=40		N=2	N=10	N=40
f1	5.9	5.9404	5.9057	5.9056	1.5	1.4313	1.4306	1.4306
f2	18.8	20.474	18.918	18.916	8.9	9.0416	8.9658	8.9655

<sup>a</sup> Exp means the experimental nature frequencies

<sup>b</sup> N means that there are N-elements used in FEM

Fig. 2.4.2 shows the frequency response of coupled model and uncoupled model.

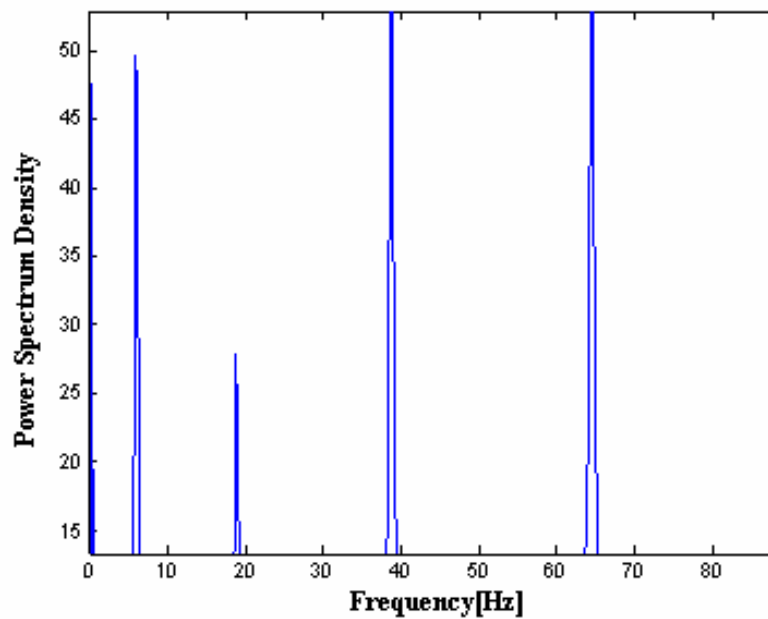


Fig. 2.4.2 (a) Coupled model frequency response

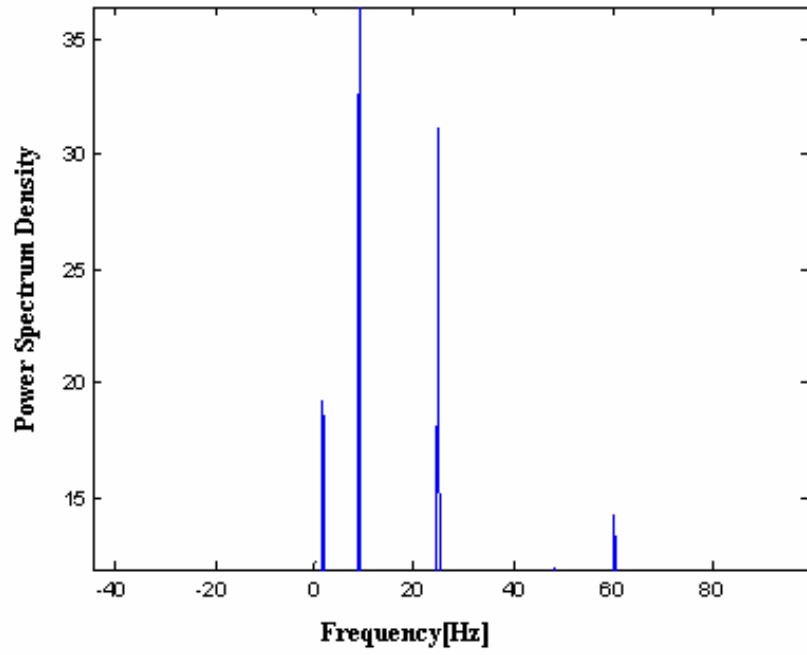


Fig. 2.4.2 (b) Uncoupled model frequency response

With the accurate flexible arm FEM model, the controller could be validly designed in the next chapter.



# Chapter 3

## Controller Design

### 3.1 Introduction

Two main classes of controllers were considered here to control the hub angle of the arm. Firstly, the flexible arm was modeled with a two-element FEM model derived in Chapter 2, and a rigid controller was developed. Then, a sliding mode controller was developed and its performance was compared with that of rigid controller. These controllers were designed to meet the following specifications:

In response to a step inputs:

1. The steady-state error must be minimized.
2. The settling time must be minimized.
3. The vibration effect of the flexible arm hub angel and tip position must be minimized.

### 3.2 Rigid Controller Design

The rigid controller is meant by considering the controller design of a rigid arm,

so the coupled terms in the FEM model, the stiffness matrix, and the mass matrix could be neglected. Then, the model is in a simple form:

$$(\mathbf{J}_R + \mathbf{M}_{\theta\theta})\ddot{\theta} = \mathbf{u} \quad (3.2.1)$$

In order to control such a double differential model, the PID controller is a candidate.

There are several well documented methods available to design PID controller.

Furthermore, PID controllers are relatively easy to implement. But in practical

Integral controller is not useful because that it may windup when the steady-state error is large and may cause damage to the transient response, such as more overshoot

or undershoot. In this experiment, the drawback of I controller was verified, so PD

controller was adapted. In order to design a suitable PD controller for the flexible arm,

the PD parameters are chosen based on the FEM model. From (3.2.1),

$$(\mathbf{J}_R + \mathbf{M}_{\theta\theta})\ddot{\theta} = \mathbf{u} = \mathbf{k}_D\dot{\theta} + \mathbf{k}_P\theta \quad (3.2.2)$$

Then, the poles placement method was used to assign the two poles to the left half

plane in s domain. Because the motor has limited maximum torque, the two poles

should be assigned to the proper position for the purpose that the input could be below

the maximum value.

### 3.3 Introduction to the Variable Structure Control (VSC)



Variable structure control (VSC) is one influential method to deal with the uncertainties of system. The structure of a VSC is a nonlinear control that switches with different control input, according to some pre-assigned algorithm or law of substructure change in the current value of the error signal and its derivatives. For example, assume there is a system

$$\ddot{x} + x = u$$

With its initial condition,

$$x(0) = 1 \quad \dot{x}(0) = 0$$

VSC is used to changing the input  $u$  in different conditions in fig.3.3.1. The response of  $x$  is better than the conditional control because VSC combines the advantages of the different inputs.

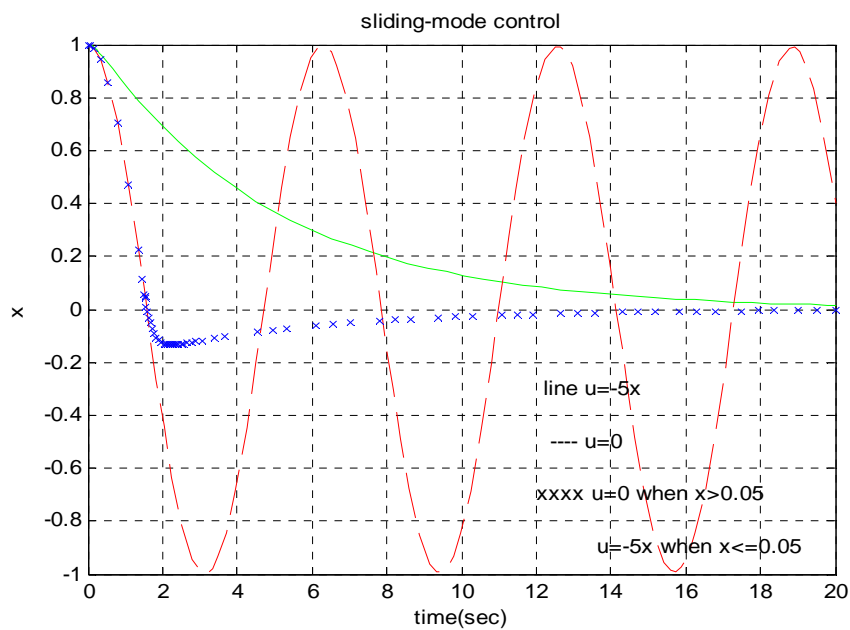
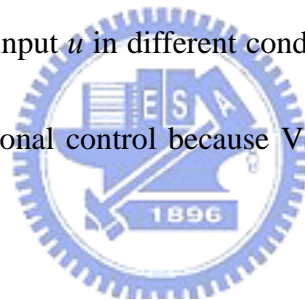


Fig. 3.3.1 Sliding Mode Control input combined with different inputs

Sliding mode control is an influential control method and is generally chosen for VSC nowadays. At first, a stable sliding surface should be determined in sliding mode control. The state variables of the system will lead to the sliding surface by variable structure control and will not leave the sliding surface. VSC is robust for the noise and disturbance and its rise time and transient response are also satisfied. Generally there are two steps in designing the sliding mode controller, the first is choosing the sliding surface, and the second is designing the sliding mode controller. The purpose of the second one is to reaching the sliding surface in limited time and it is easier to achieve than the first. Choosing a good sliding surface is an art.



### 3.4 Sliding Mode Controller Design

The purpose of this experiment is to rotate the flexible arm to the desired angle  $\theta_d$  and eliminate the vibration of the arm. So the state variables of the FEM should be brought to zero finally, in the beginning, the controllability of the plant model must be checked out. From (2.2.17), because  $\mathbf{M}$  is positive definite matrix that its inverse matrix is exist.

$$\dot{\mathbf{x}} = \mathbf{Ax} + \mathbf{Bu} \quad (3.4.1)$$

Where  $\mathbf{x} = [\theta \quad v_1 \quad \cdots \quad v_{2N} \quad \dot{\theta} \quad \dot{v}_1 \quad \cdots \quad \dot{v}_{2N}]$  (3.4.2)

$$A = \begin{bmatrix} 0 & I \\ -M^{-1}K & 0 \end{bmatrix} \quad (3.4.3)$$

$$B = \begin{bmatrix} 0 \\ M^{-1}b_N \end{bmatrix} \quad (3.4.4)$$

PBH test shows that  $(A, B)$  is controllable if and only if  $\text{rank}(\lambda I - A - B)$  is full rank for all eigenvalues  $\lambda$ . After checking all the eigenvalues, the result shows that the flexible arm FEM model is controllable and could be used poles placement method to design the controller. Then, design the error states as

$$e_1 = \theta - \theta_d \quad (3.4.5)$$

$$e_2 = v_1 - x_{1d}$$

⋮

$$e_{2N+2} = x_{2N+2} - x_{(2N+2)d}$$



Substituting (3.4.5) into (2.2.17) yields

$$M\ddot{E} + KE + KD = Bu \quad (3.4.6)$$

where  $E = [e_1 \ e_2 \ \dots \ e_{2N+2}]'$  (3.4.7)

$$D = [\theta_d \ 0 \ \dots \ 0]' \quad (3.4.8)$$

Then  $\dot{Z} = AZ + Bu + dD$  (3.4.9)

where  $Z = \begin{bmatrix} E \\ \dot{E} \end{bmatrix}$  (3.4.10)

$$d = \begin{bmatrix} 0 \\ -M^{-1}K \end{bmatrix} \quad (3.4.11)$$

Although there are some documents mentioned about the global damping matrix in

dynamic equation [12], we still neglect the phenomenon because the effect is not very clear. In order to design the sliding mode controller, sliding surface  $\mathbf{S} = \mathbf{C}\mathbf{x}$  is need to be chosen at first. The sliding surface in our design is based on Lyapunov method shown in Appendix C. assume the sliding Surface is expressed as

$$\mathbf{s} = \mathbf{C}^T \mathbf{Z} \quad (3.4.12)$$

where  $\mathbf{C}$  is the sliding surface coefficient chosen in Appendix C [16]. The equivalent control input could be obtained from

$$\dot{\mathbf{s}} = \mathbf{C}^T \dot{\mathbf{Z}} \quad (3.4.13)$$

Substituting (3.4.9) into (3.4.12) yields

$$\dot{\mathbf{s}} = \mathbf{C}^T \mathbf{A}\mathbf{Z} + \mathbf{C}^T \mathbf{B}\mathbf{u}_{eq} + \mathbf{C}^T d\mathbf{D} \quad (3.4.14)$$

$$\mathbf{u}_{eq} = -(\mathbf{C}^T \mathbf{B})^{-1} (\mathbf{C}^T \mathbf{A}\mathbf{Z} + \mathbf{C}^T d\mathbf{D}) \quad (3.4.15)$$

The controlled system's sliding motion now is restricted by

$$\dot{\mathbf{Z}} = \left( \mathbf{I} - \mathbf{B}(\mathbf{C}^T \mathbf{B})^{-1} \mathbf{C}^T \right) \mathbf{A}\mathbf{Z} + \left( \mathbf{I} - \mathbf{B}(\mathbf{C}^T \mathbf{B})^{-1} \mathbf{C}^T \right) d\mathbf{D} \quad (3.4.16)$$

$$\mathbf{s} = \mathbf{C}^T \mathbf{Z} = 0 \quad (3.4.17)$$

According to (3.4.17), the order of the system is reduced by one. In order to guarantee that the trajectory of the states will enter the sliding surface, the control law must satisfied the reaching and sliding condition

$$\mathbf{s}\dot{\mathbf{s}} < 0 \quad (3.4.18)$$

Substituting (3.4.14) into (3.4.18) yields

$$s\dot{s} = s(C^T AZ + C^T Bu_{eq} + C^T dD) \quad (3.4.19)$$

If the control law is set as

$$u = -(C^T B)^{-1}(C^T AZ + C^T dD + \text{sgn}(s)k) \quad (3.4.20)$$

where

$$k > 0$$

$$\text{sgn}(s) = \begin{cases} 1 & \text{if } s > 0 \\ -1 & \text{if } s < 0 \end{cases} \quad (3.4.21)$$

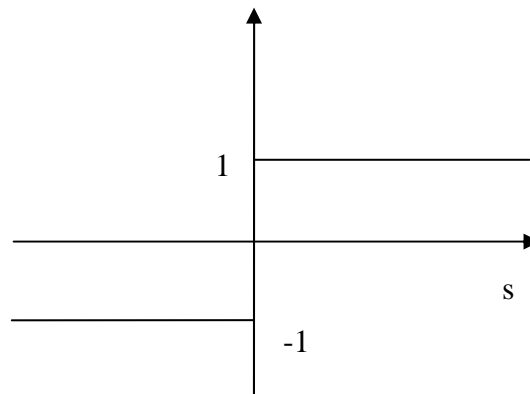


Fig. 3.4.1  $\text{Sgn}(s)$  function

The condition (3.4.18) will be met because

$$s\dot{s} = -ks \text{sgn}(s) = -k|s| \quad (3.4.18)$$

When the control law (3.4.15) is applied, using sign function  $\text{sgn}(s)$  will cause chattering effect which could be eased off by Slotine's boundary-layer modification.

We use the saturation function

$$sat(s) = \begin{cases} sgn(s) & \text{if } |s| > \varepsilon \\ s / \varepsilon & \text{if } |s| \leq \varepsilon \end{cases} \quad (3.4.22)$$

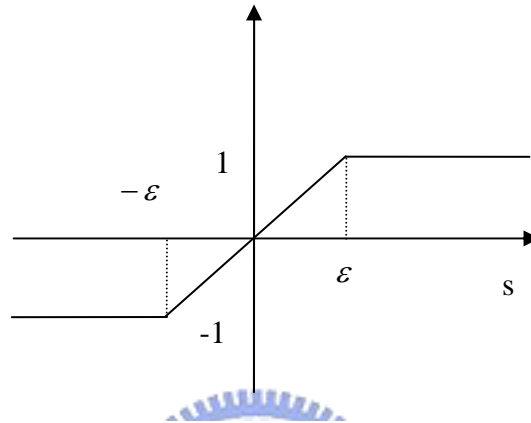


Fig. 3.4.2  $Sat(s)$  function

substituted for sign function  $sgn(s)$ . Therefore, the control law is rewritten as

$$\mathbf{u} = -(\mathbf{C}^T \mathbf{B})^{-1} (\mathbf{C}^T \mathbf{A} \mathbf{Z} + \mathbf{C}^T \mathbf{d} \mathbf{D} + sat(s) \mathbf{k}) \quad (3.4.23)$$

Before entering the sliding layer  $|s| > \varepsilon$ , the modified control law is the same as the previous one. The control law forces the system trajectory to reach the sliding layer  $|s| \leq \varepsilon$  in a limit time. When entering the sliding layer, gain of the control law must be minimized. And, the system can't maintain zero when there occurs a disturbance. It means that the control law couldn't make all states to zero but around zero. The tradeoff of the decreased precision is that the input chattering effect is slow down and input gain is decreased. The key point is that the sign function of (3.4.20) is not

realizable in practical because of its infinite switch, and the modified control input

(3.4.23) could be realized in practical component.



# Chapter 4

## Simulation Results

### 4.1 Pole Placement

From Chapter 2, two-element model is chosen as the desired control system [11], and the flexible model has 10 system poles shown in Fig. 4.1.1. Before system simulation, the desired system poles should be determined first. In rigid control, the poles  $-0.5$  and  $-2$  are determined and used in experimental demonstration. Then, consider about the Sliding mode control, Lyapunov method which has been introduced in Appendix C is used to design the sliding surface. The system poles of the control system should be designed in the procedure of applying Lyapunov method. The desired poles for sliding mode control are shown in Fig. 4.1.2. The dominant poles of SMC are designed at  $-0.5$  and  $-2$ , and the other poles are designed as complex conjugates lined in  $45$  degrees to the origin in left half plane. The imaginary part of original poles (Fig. 4.1.1) and desired poles (Fig. 4.1.2) are of the same value, so that the sliding surface will let the controller better with low input torque. But, the shortcoming of the Lyapunov method is that the finally poles of the system may not be the same position as we expected in controller design when the control goal is



achieved which is meant that the system is in sliding surface. However, there is a significant advantage of the Lyapunov method based on its fundamental algorithm which is come from energy for the sliding surface design yields the less input torque required. Not only consider about the limited motor torque in this experiment but also concern for power consumption, Lyapunov method achieves a good result in input restricted torque compared with the transformation matrix method. As for PD controller, it also needs large torque for better transient response [5]. Although the worse case could be corrected by adding a shaping reference input [13, 4].

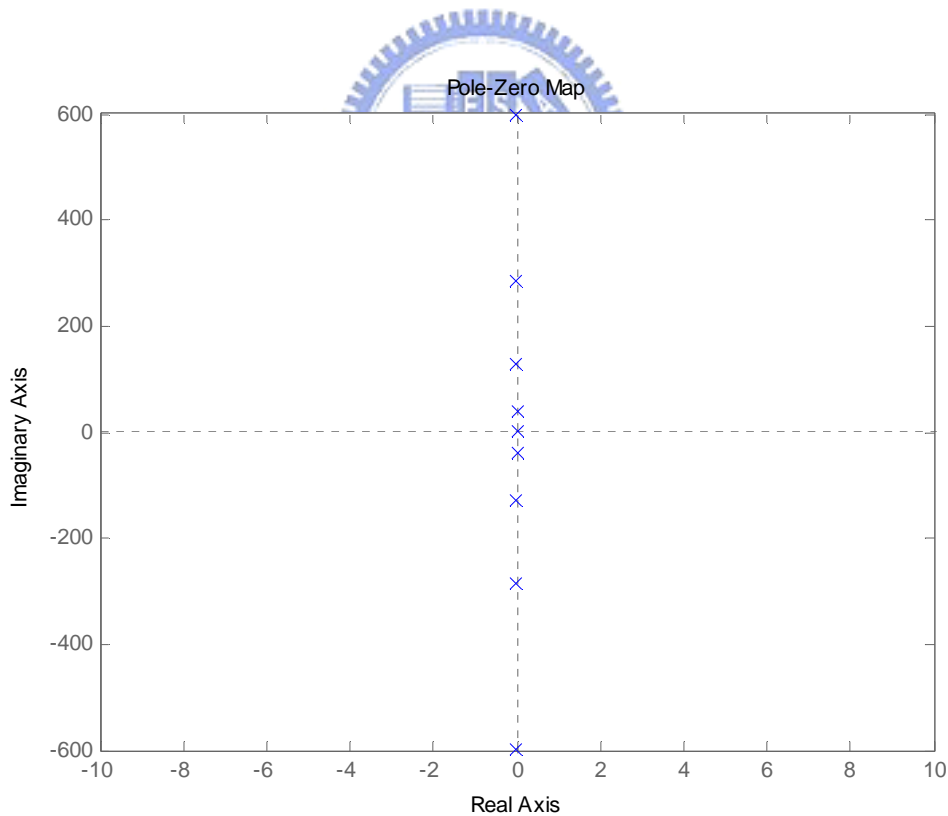


Fig. 4.1.1 The system poles of the flexible arm

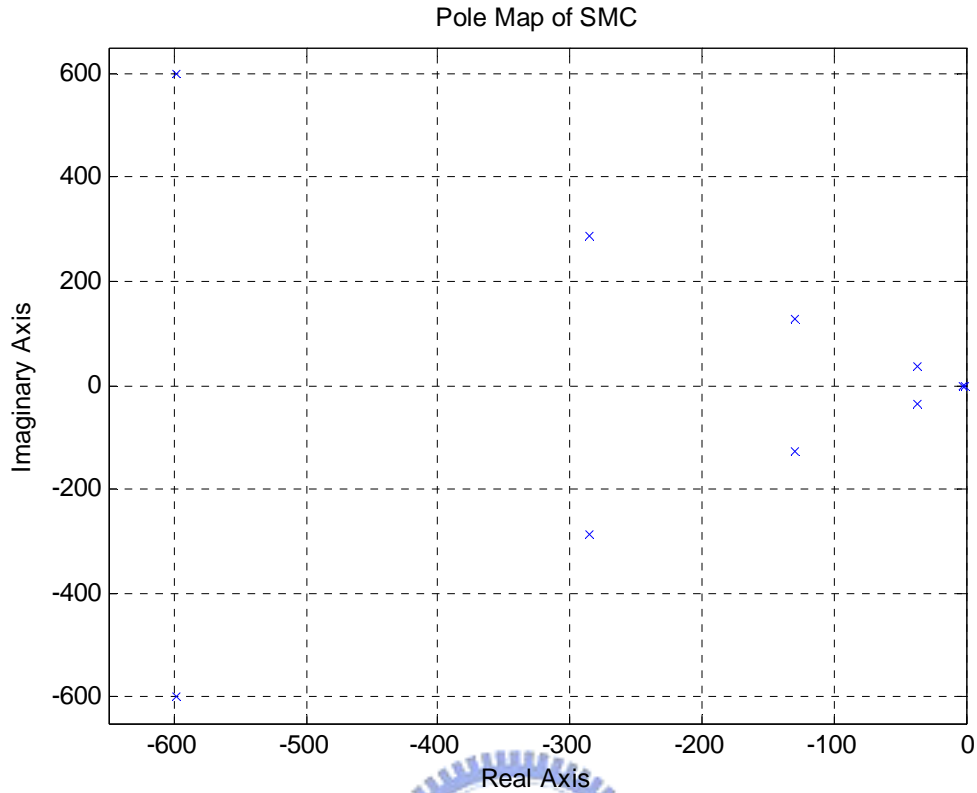


Fig. 4.1.2 The desired poles of the sliding mode controller

#### 4.2 Sliding Mode Controller Simulation Results

According to poles placement in section 4.1, the system poles are determined in sliding mode control. Then, the software Matlab is used to verify the controller. With the experimental equipment parameters showed in Table 2.4.1, the simulation results for hub angle regulation are shown in Fig. 4.2.1 to Fig. 4.2.5, and the parameters  $\varepsilon = 0.01$  and  $\sigma = 5$ .

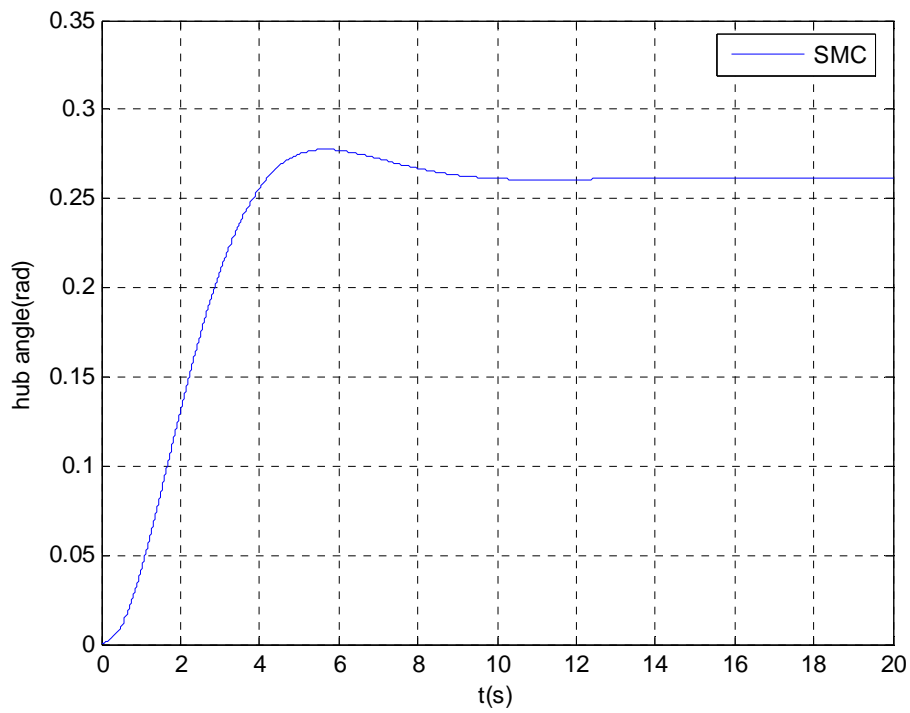


Fig. 4.2.1 Hub angle regulation in sliding mode control

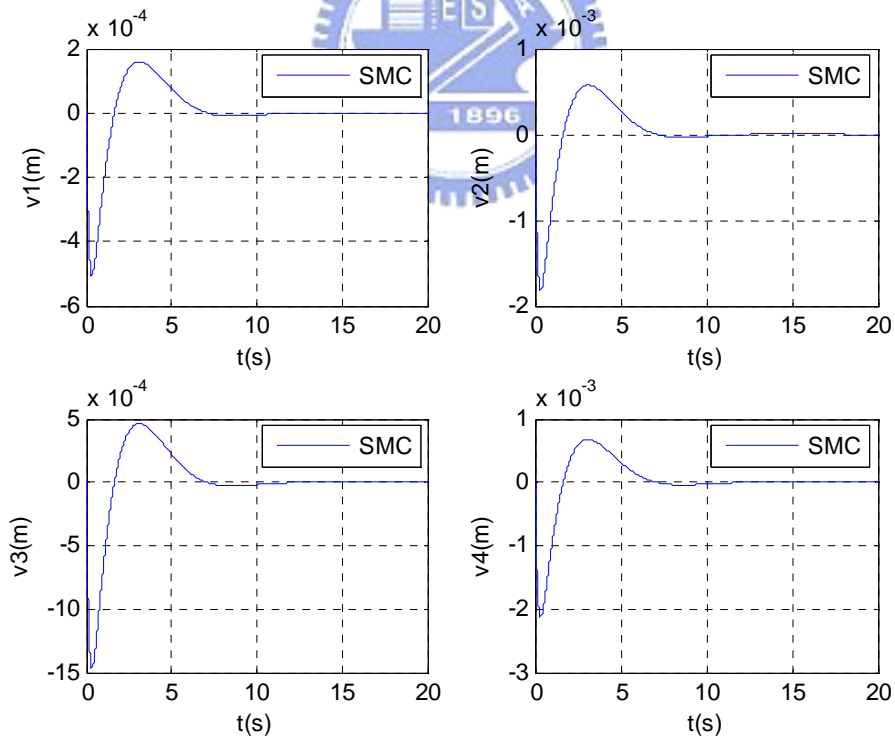


Fig. 4.2.2 Four states response in sliding mode control

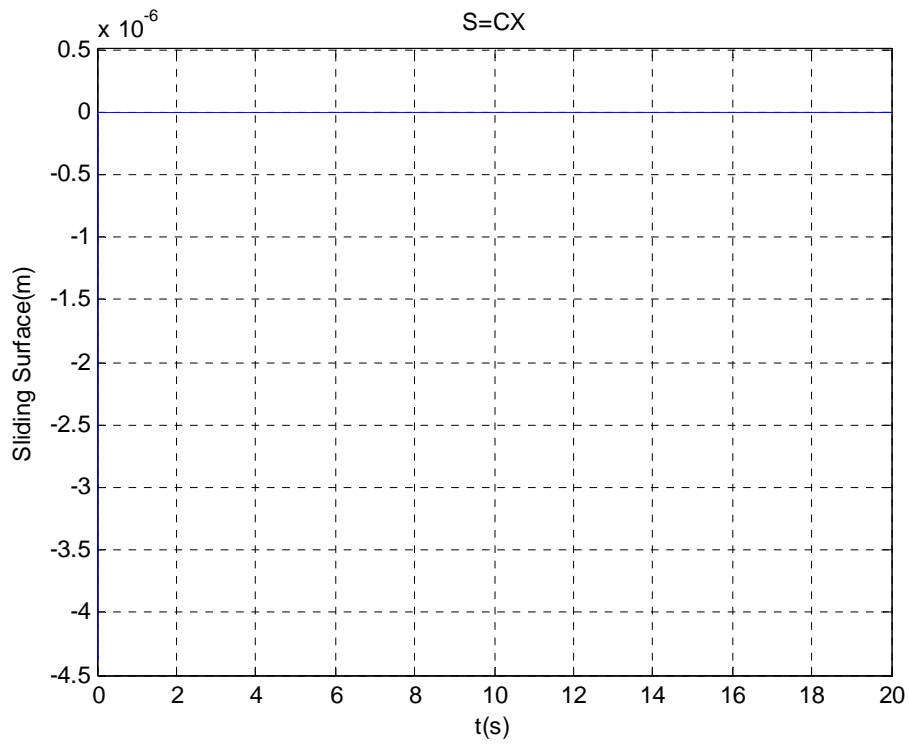


Fig. 4.2.3 Sliding surface in sliding mode control

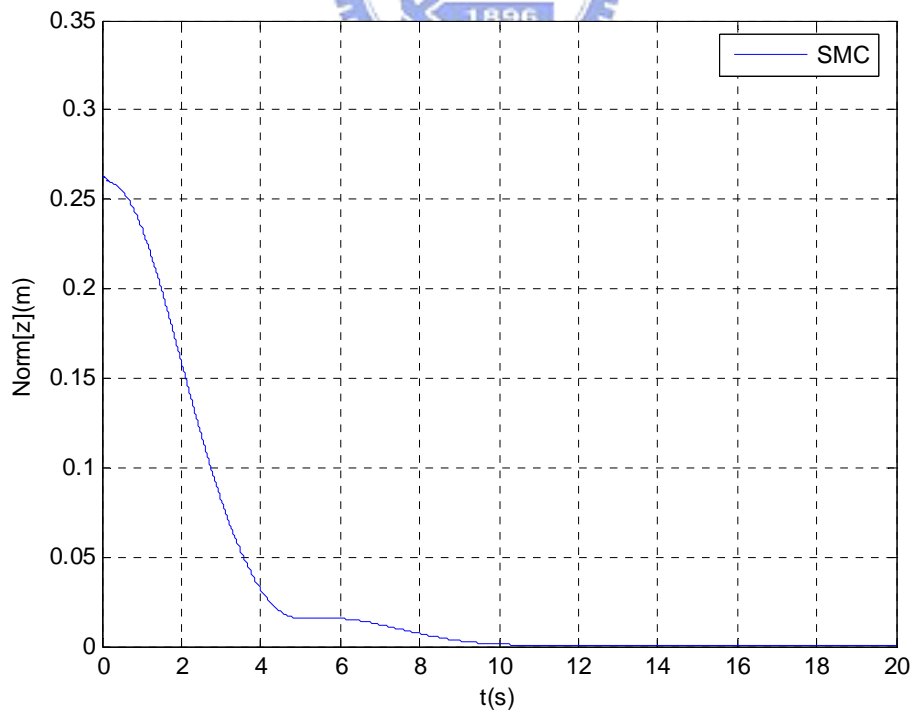


Fig. 4.2.4 Norm of the error states in sliding mode control

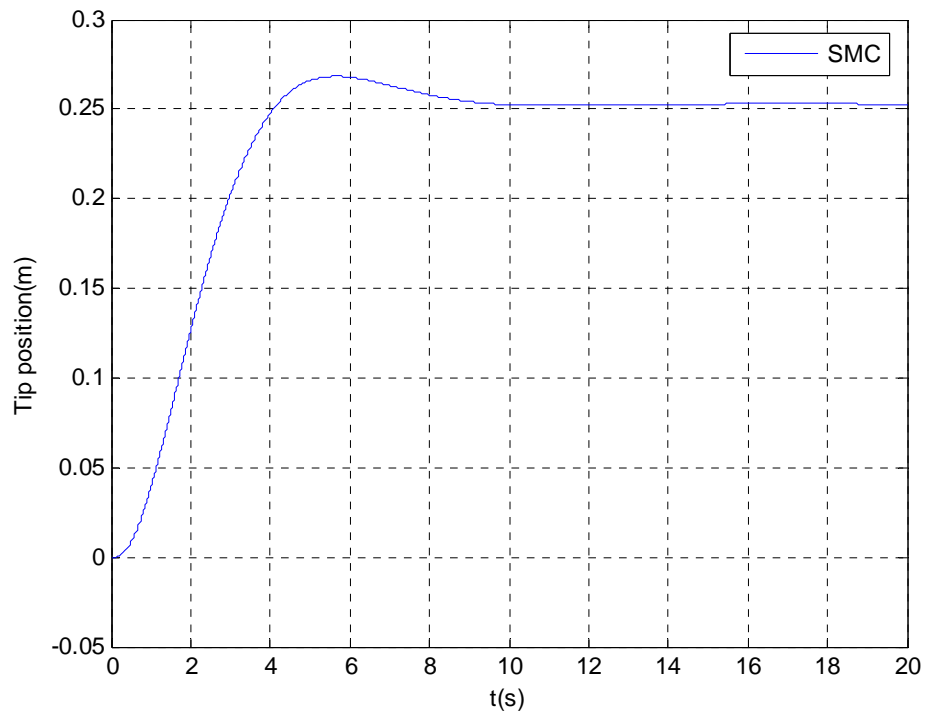


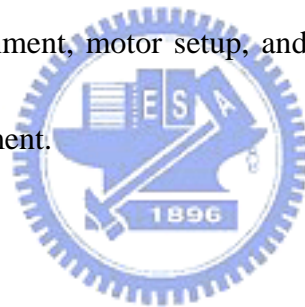
Fig. 4.2.5 Tip position regulation in sliding mode control

We have considered the sliding mode controller for the flexible arm. A set of simulation has been carried out. Simulation results confirm that the controller performs remarkably well with suppressed vibration.

# Chapter 5

## Experimental Demonstration

This chapter is about the flexible arm experimental demonstration. The results will show the sliding mode controller is successful in vibration tolerance and the developed FEM model of the flexible arm is valid. Compared with the simulation results, the experimental demonstration makes us convinced of the controller design in chapter is work. The beginning of this chapter is about experiment setup included of Matlab xPC target environment, motor setup, and deflection measurement which are the foundations of experiment.



### 5.1 Experimental Setup

#### 5.1.1 Matlab xPC Target Environment

This experiment is established in Matlab toolbox-xPC Target. In Fig.5.1.1, xPC-MC240 I/O card is used to get the angle from the motor and PCI-1716 card is used to do AD/DA signal convert. The xPC Target is a solution for prototyping, testing, and deploying real-time systems using standard PC hardware. It is an

environment that uses a target PC, separate from a host PC, for running real-time applications. In this environment the desktop computer as a host PC with Matlab and Simulink creates a model using Simulink blocks. After creating the model, xPC Target lets the blocks and a C/C++ compiler to create executable code with its embedded coder. The executable code is downloaded from the host PC to the target PC running the xPC Target real-time kernel. After downloading the executive code, the application can be run by the target PC in real-time. The advantages of xPC Target are the fast sampling rate to ten thousands Hz in real-time work and it is convenient to hardware implementation with convenient parameters turning.

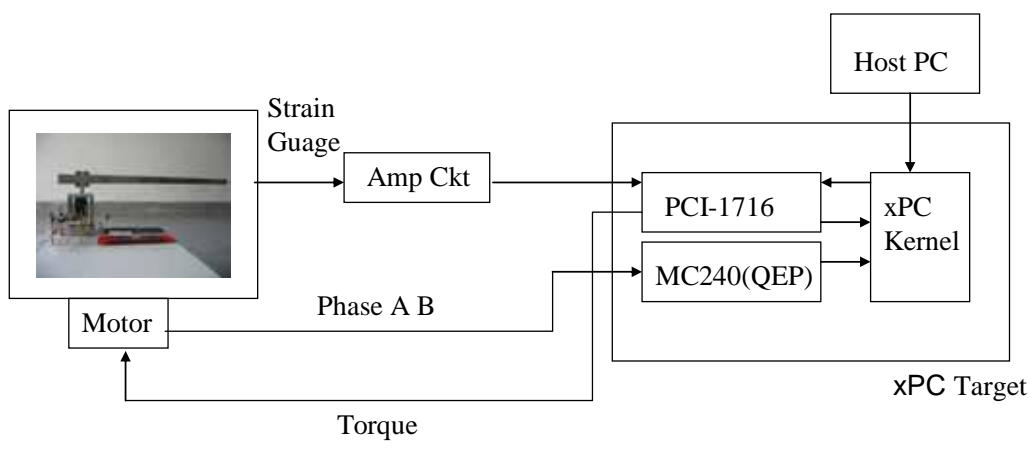


Fig. 5.1.1 Hardware Architecture

### 5.1.2 Motor Setup

The Mitsubishi AC-servo motor HC-KFS 053B and the servo-amplifier MR-J2S-10A are adapted in the experiment. The specifications of AC-servo motor HC-KFS 053B is shown below in the table 5.1.2 [20].

Table 5.1.2 Servo Motor Specifications

Maximum torque	0.48[Nm]
Maximum rotation speed	3000[rpm]
Moment of inertia $J$	$0.053[\times 10^{-4} \text{kgm}^2]$
Position detector	131072p/rev[17-bits]
Maximum current	2.5[A]
Rated current	0.83[A]
Permissible instantaneous rotation speed	5175[r/min]
Maximum rotation speed	4500[rpm]



The PCI-1716 card provides a 16-bit resolution AD/DA transformation for strain feedback and torque driven voltage. The hub angle is detected by the xPC-MC240 I/O card with a TM S320F240DSP embedded with Quadrature Encoder Pulse (QEP) circuit. The QEP circuit determines the rotation direction by the input generated by an optical encoder on a motor shaft, the direction of rotation of the motor can be determined by detecting which of the two sequences leads. The two sequences are pulses with variable frequencies and fixed phase shifts of a quarter of a period (90 degrees). The angular position and speed can be determined by the pulse count.



High-resolution position determination 32768 pulse per revolution is applied in this experiment.

### 5.1.3 Deflection Measurement

Several methods have been used to measure the deflections of the arm, such as Photo-Diodes, Laser Doppler Vibrometers, and Strain gauges. Since strain gauges are cheap and effective sensors, they are used to measure strains as small as a few  $\mu\epsilon$  in this experiment. A strain gauge is basically a grid of wire or conductor attached to the arm and changes its conductance as the arm stretches. This change in conductance is used to find the change in bending moment of the arm. The strain  $\epsilon$  measured in the arm is related to the deflection  $w(x, t)$  as follows [10]:

$$\epsilon = \frac{1}{2} \frac{\partial^2 w(x, t)}{\partial x^2} \Big|_{x=p} + \frac{1}{2} \left( \left( \frac{\partial w}{\partial x} \Big|_{x=p} \right)^2 + \left( \frac{\partial^2 w}{\partial^2 x} \Big|_{x=p} \right)^2 \right) \quad (5.1)$$

where  $x$  is the axis parallel to the arm in a stress-free state and  $p$  is the distance between the location strain gauge attached and the root of the arm. However, the disadvantage of the strain gauges is that they have a maximum strain and might get damaged subject to higher strains. Only small deflections in the arm are considered. The strain-gauge KYOWA Y3099 is used in this experiment.

To precisely detect the distortion of the arm, first determine a certain positions with explicit deformation and then purposely paste two strain gauges to each of these positions in the way of face-to-face on both sides. When deformation appears, the resistance of each strain gauge changes with the variation  $\Delta R$ . The small variation  $\Delta R$  will be detected by the Wheatstone bridge circuit shown in Fig. 5.1.2.

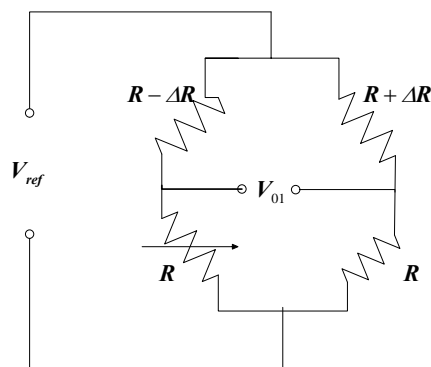


Fig.5.1.2 Wheatstone Bridge Circuit

The gain of the Wheatstone bridge circuit is

$$V_{o1} = V_{ref} \frac{2R\Delta R}{4R^2 - \Delta R^2} \quad (5.2)$$

The value of  $V_{o1}$  is small in (5.2) because of the use of low voltage  $V_{ref}$  to protect the strain gauges from broken by high temperature due to the high reference voltage.

In this experiment, the reference voltage  $V_{ref}$  is assigned to 5 volt. The voltage

amplifier circuit shown in Fig. 5.1.3 is designed to amplify  $V_{o1}$  so that the AD input will get higher resolution.

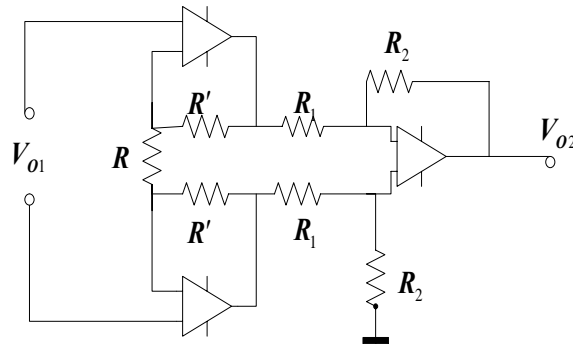


Fig.5.1.3 Voltage Amplifier Circuit

The circuit of Fig.5.1.3 which is common used as an industrial voltage amplifier has high input resistance and good CMRR. The  $V_{o2}$  could be calculated as

$$V_{o2} = \left(1 + \frac{2R'}{R}\right) \frac{R_2}{R_1} \times V_{o1} \quad (5.3)$$

When the resistances  $R$ ,  $R'$ ,  $R_1$ , and  $R_2$  are chosen in proper values, the proper gain which limits the A/D input ranged inside  $\pm 10V$  could be achieved. Finally, it is important to design a low pass filter to reduce the high pass noise. The second order Butterworth filter shown in Fig.5.1.4 is designed and its 3db cutoff frequency assigned to 250Hz is calculated in (5.4). The frequency response of the filter is shown in Fig.5.1.5.

$$H(s) = \frac{V_{o3}}{V_{o2}} = \frac{1}{(C_1 C_2 R_1 R_2) s^2 + C_2 (R_1 + R_2) s + 1} \quad (5.4)$$

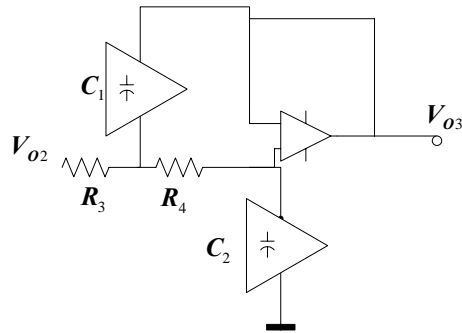


Fig.5.1.4 Low Pass Filter Circuit

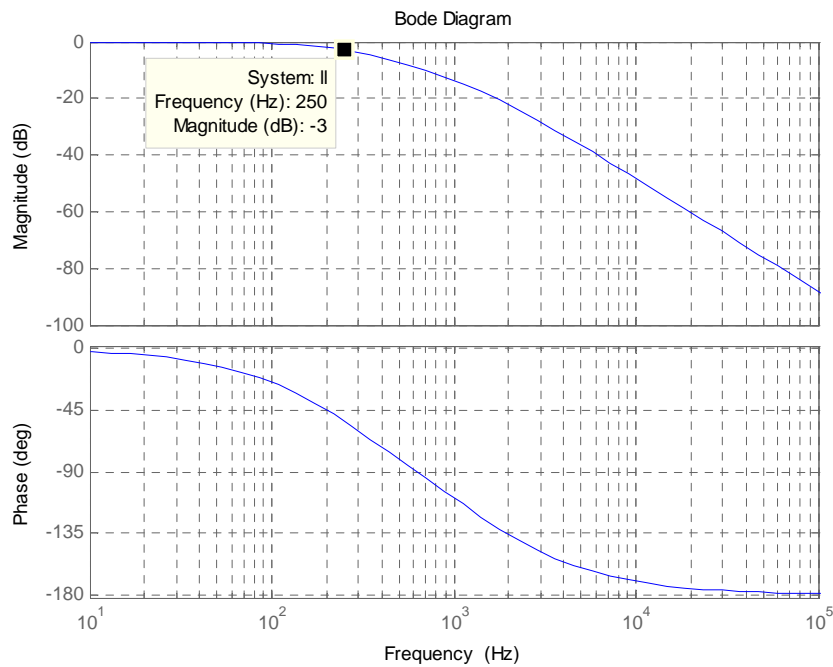


Fig.5.1.5 Low Pass Filter Bode Plot

Although the low pass filter is designed in the last stage of the circuit, there is still

some high impulse noise appears when signal transfers in wires, but it is solved by a software 80Hz low pass filter in digital before into the digital controller. Until now, the signals of strain gauges are finally precisely fed back. However, the state feedback is considered as elements' position angular variation and angular velocity, so the mathematical transformation from strain gauges feedback to states needs to derived. Here, the mathematical transformation in two-element FEM model is considered and will be shown in the following description. By definitions, the measured amount for a strain gauge feedback is an external moment applied to a strain gauge position. The

first strain gauges pasted at  $x_1$  to the root can be described as

$$\frac{\partial^2 w_1(x_1, t)}{\partial x_1^2} = \mu \cdot M_1 \quad (5.5)$$

The second ones pasted at  $x_2$  to the root can be described as

$$\frac{\partial^2 w_2(x_2, t)}{\partial x_2^2} = \mu \cdot M_2 \quad (5.6)$$

Consider the continuous boundary between two elements, the moment of them must be the same, so

$$\frac{\partial^2 w_1(h, t)}{\partial x_1^2} = \frac{\partial w_2(0, t)}{\partial x_2^2} \quad (5.7)$$

And, the principle assumption of Euler Bernoulli beam is the zero moment at the arm tip, so

$$\frac{\partial^2 w_2(h, t)}{\partial x_2^2} = 0 \quad (5.8)$$

Then, substituting  $w(x, t)$  into (5.5) (5.6) (5.7) (5.8) yields

$$\frac{\partial^2 \mathbf{w}_1(\mathbf{x}_1, \mathbf{t})}{\partial \mathbf{x}_1^2} = \mu \cdot \mathbf{M}_1$$

$$\phi_1''(\mathbf{x}_1) \cdot 0 + \phi_2''(\mathbf{x}_1) \cdot 0 + \phi_3''(\mathbf{x}_1) \cdot \mathbf{v}_1(\mathbf{t}) + \phi_4''(\mathbf{x}_1) \cdot \mathbf{v}_2(\mathbf{t}) = \mu \mathbf{M}_1 \quad (5.9)$$

$$\frac{\partial^2 \mathbf{w}_2(\mathbf{x}_2, \mathbf{t})}{\partial \mathbf{x}_2^2} = \mu \cdot \mathbf{M}_2$$

$$\phi_1''(\mathbf{x}_2) \cdot \mathbf{v}_1(\mathbf{t}) + \phi_2''(\mathbf{x}_2) \cdot \mathbf{v}_2(\mathbf{t}) + \phi_3''(\mathbf{x}_2) \cdot \mathbf{v}_3(\mathbf{t}) + \phi_4''(\mathbf{x}_2) \cdot \mathbf{v}_4(\mathbf{t}) = \mu \mathbf{M}_2 \quad (5.10)$$

$$\frac{\partial^2 \mathbf{w}_1(\mathbf{h}, \mathbf{t})}{\partial \mathbf{x}_1^2} = \frac{\partial \mathbf{w}_2(0, \mathbf{t})}{\partial \mathbf{x}_2^2}$$

$$\phi_3''(\mathbf{h}) \cdot \mathbf{v}_1(\mathbf{t}) + \phi_4''(\mathbf{h}) \cdot \mathbf{v}_2(\mathbf{t}) = \phi_1''(0) \cdot \mathbf{v}_1(\mathbf{t}) + \phi_2''(0) \cdot \mathbf{v}_2(\mathbf{t}) + \phi_3''(0) \cdot \mathbf{v}_3(\mathbf{t}) + \phi_4''(0) \cdot \mathbf{v}_4(\mathbf{t}) \quad (5.11)$$

$$\frac{\partial^2 \mathbf{w}_2(\mathbf{h}, \mathbf{t})}{\partial \mathbf{x}_2^2} = 0$$

$$\phi_1''(2\mathbf{h}) \cdot \mathbf{v}_1(\mathbf{t}) + \phi_2''(2\mathbf{h}) \cdot \mathbf{v}_2(\mathbf{t}) + \phi_3''(2\mathbf{h}) \cdot \mathbf{v}_3(\mathbf{t}) + \phi_4''(2\mathbf{h}) \cdot \mathbf{v}_4(\mathbf{t}) = 0 \quad (5.12)$$

Rearrange (5.9) (5.10) (5.11) (5.12) into a matrix form

$$\phi \cdot \mathbf{v} = \mu \cdot \mathbf{M} \quad (5.13)$$

where

$$\phi = \begin{bmatrix} \phi_3''(\mathbf{x}_1) & \phi_4''(\mathbf{x}_1) & 0 & 0 \\ \phi_1''(0) - \phi_3''(\mathbf{h}) & \phi_2''(0) - \phi_4''(\mathbf{h}) & \phi_3''(0) & \phi_4''(0) \\ \phi_1''(\mathbf{x}_2) & \phi_2''(\mathbf{x}_2) & \phi_3''(\mathbf{x}_2) & \phi_4''(\mathbf{x}_2) \\ \phi_1''(2\mathbf{h}) & \phi_2''(2\mathbf{h}) & \phi_3''(2\mathbf{h}) & \phi_4''(2\mathbf{h}) \end{bmatrix} \quad (5.14)$$

$$\mathbf{v} = \begin{bmatrix} \mathbf{v}_1(\mathbf{t}) \\ \mathbf{v}_2(\mathbf{t}) \\ \mathbf{v}_3(\mathbf{t}) \\ \mathbf{v}_4(\mathbf{t}) \end{bmatrix} \quad (5.15)$$

$$\mathbf{M} = \begin{bmatrix} \mathbf{M}_1 \\ 0 \\ \mathbf{M}_2 \\ 0 \end{bmatrix} \quad (5.16)$$

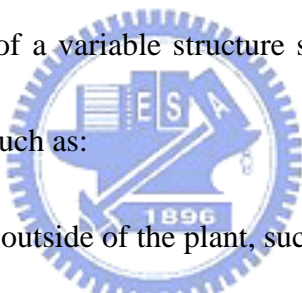
When  $\phi^{-1}$  is exist, the flexible arm state variables could be calculated by

$$\mathbf{v} = \mu \cdot \phi^{-1} \cdot \mathbf{M} \quad (5.17)$$

Now, we have already described the measurement the strain moments of two elements of the arm.

## 5.2 Sliding Mode Controller Experimental Results

Consider the robustness of a variable structure system, there are three kinds of noises need to be faced [15]. Such as:

- 
- A. The disturbance from outside of the plant, such as AC power supply ...etc.
  - B. The uncertainty of the system parameters changes with different environment, such as changes of temperature.
  - C. The unmodeled modes are hard to find in the control system.

As a result, Fig. 5.2.1 to Fig. 5.2.3 show the experimental results of the flexible arm controlled by a rigid controller whose poles designed in -0.5 and -2. This demonstration shows that these disturbances yield much vibration in rigid controller. We needs to avoid these noises carefully, or the control goal may be failed, even then the system will get loss in preciseness and be unstable. So how to arise the robustness

of the control system is an important target in system and controller design. Variable structure control is well used in practical for the most part of its robustness. The hub regulation experimental results shown in Fig. 5.2.4 to Fig. 5.2.15 also verify the advantages of SMC. In these figures, the dominant poles of SMC are designed at  $-0.5$  and  $-2$ , and the other poles are designed as complex conjugates lined in  $45$  degrees to the origin in left half plane shown in Fig.4.1.1. In Fig.5.2.4 to Fig. 5.2.7, the parameters are defined as  $\varepsilon = 0.01$  and  $\sigma = 5$ . Then, in Fig.5.2.8 to Fig. 5.2.11, the parameters are defined as  $\varepsilon = 0.0067$  and  $\sigma = 6$ . Finally, in Fig.5.2.12 to Fig. 5.2.15, the parameters are defined as  $\varepsilon = 0.005$  and  $\sigma = 8$ .

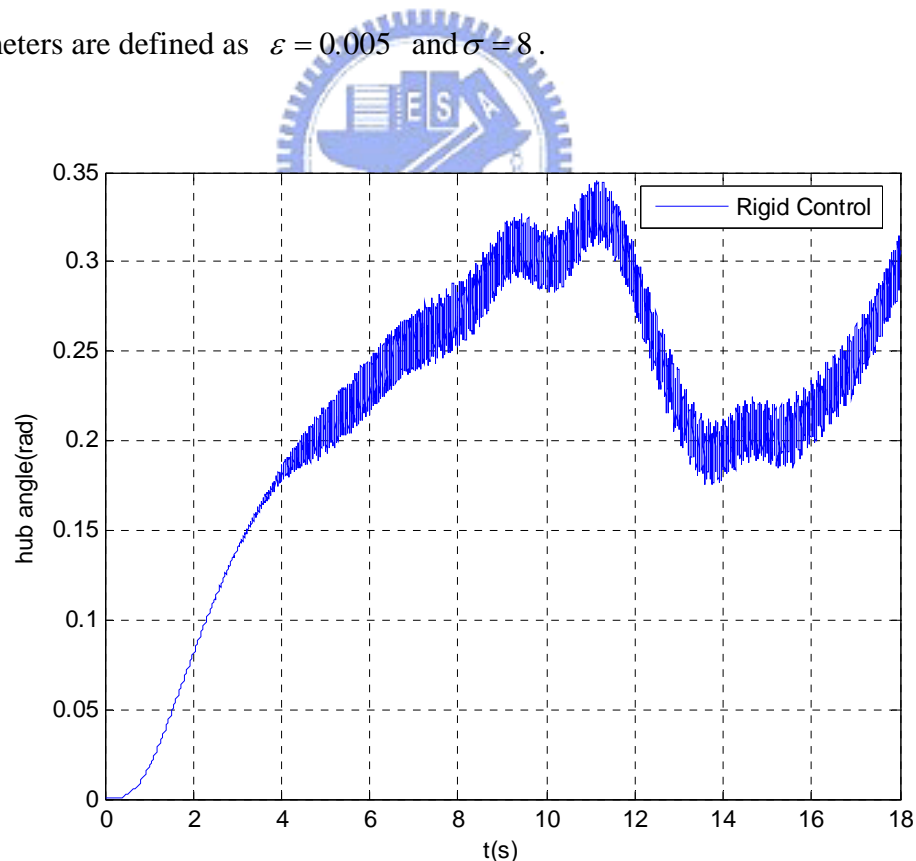


Fig. 5.2.1 Hub angle regulation in rigid control



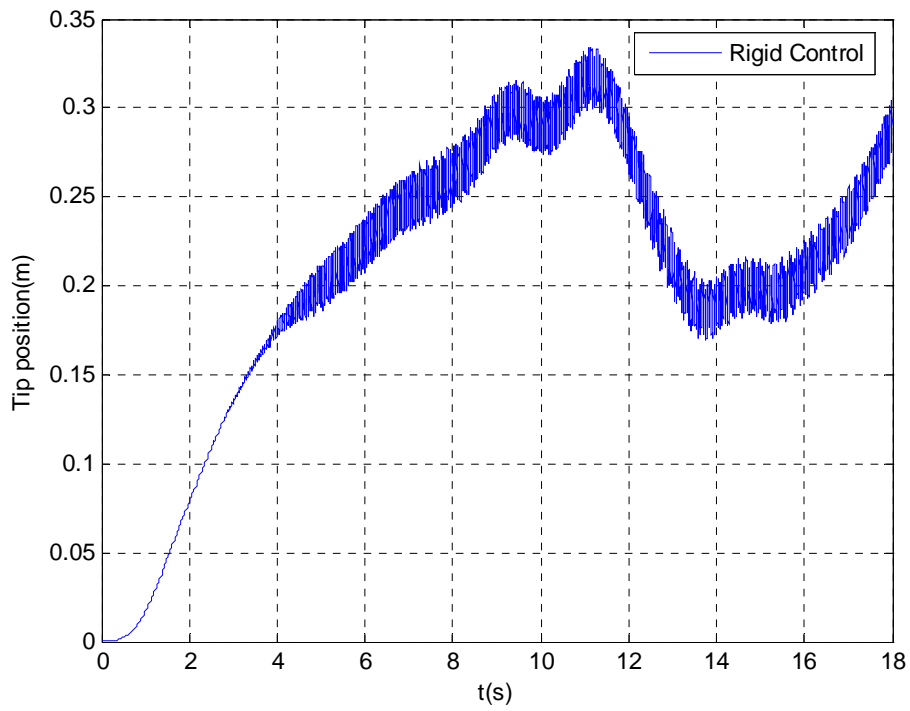


Fig. 5.2.2 Tip position regulation in rigid control

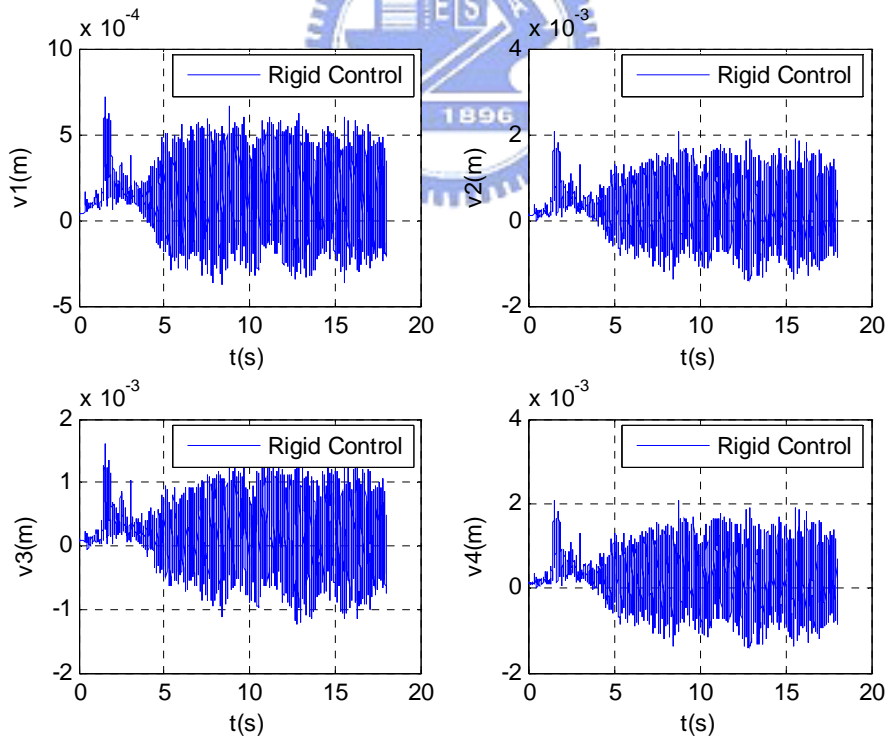


Fig. 5.2.3 Four states response in rigid control

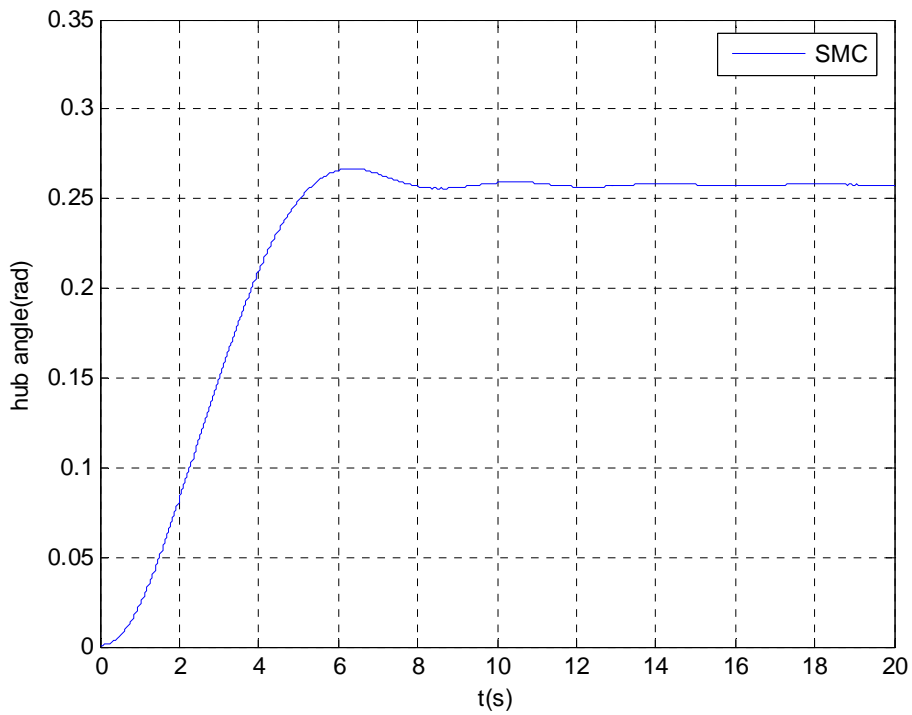


Fig. 5.2.4 Hub angle regulation in sliding mode control ( $\varepsilon = 0.01$  and  $\sigma = 5$ )

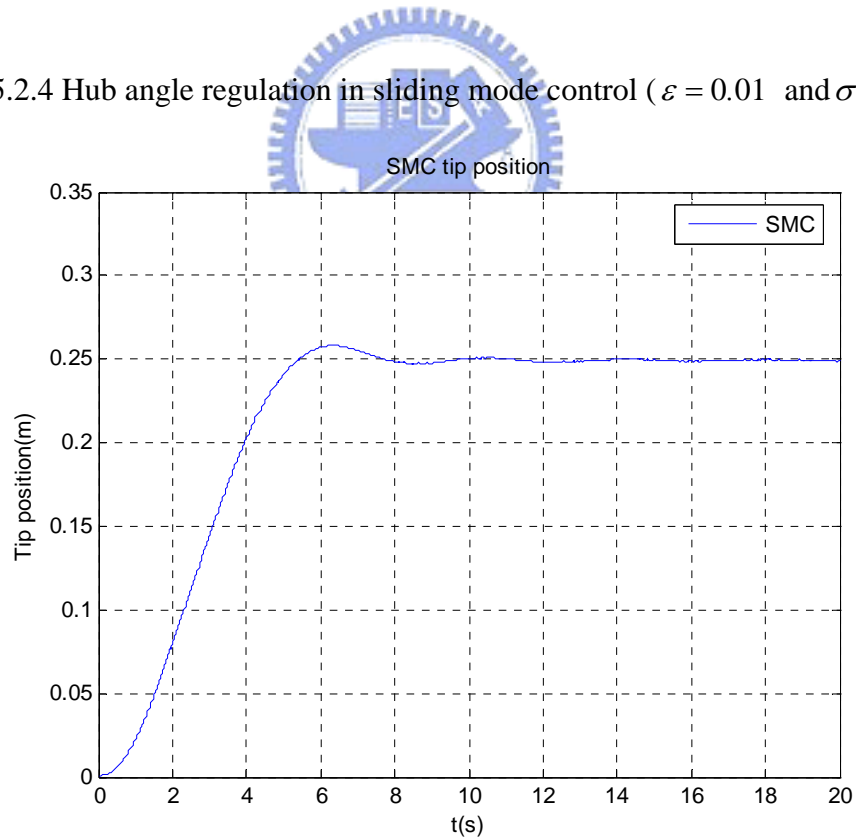


Fig. 5.2.5 Tip position regulation in sliding mode control ( $\varepsilon = 0.01$  and  $\sigma = 5$ )

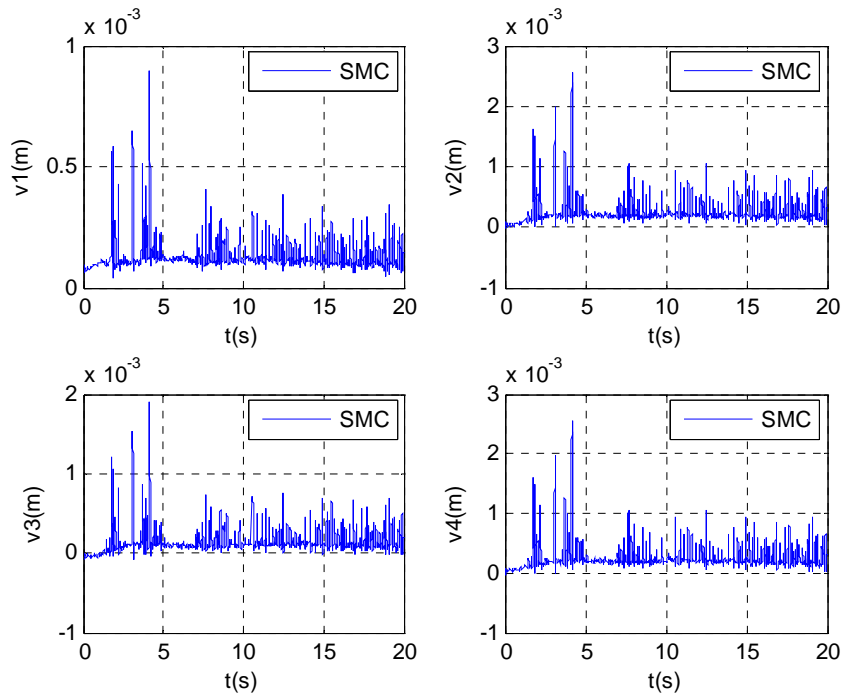


Fig. 5.2.6 Four states response in sliding mode control ( $\varepsilon = 0.01$  and  $\sigma = 5$ )

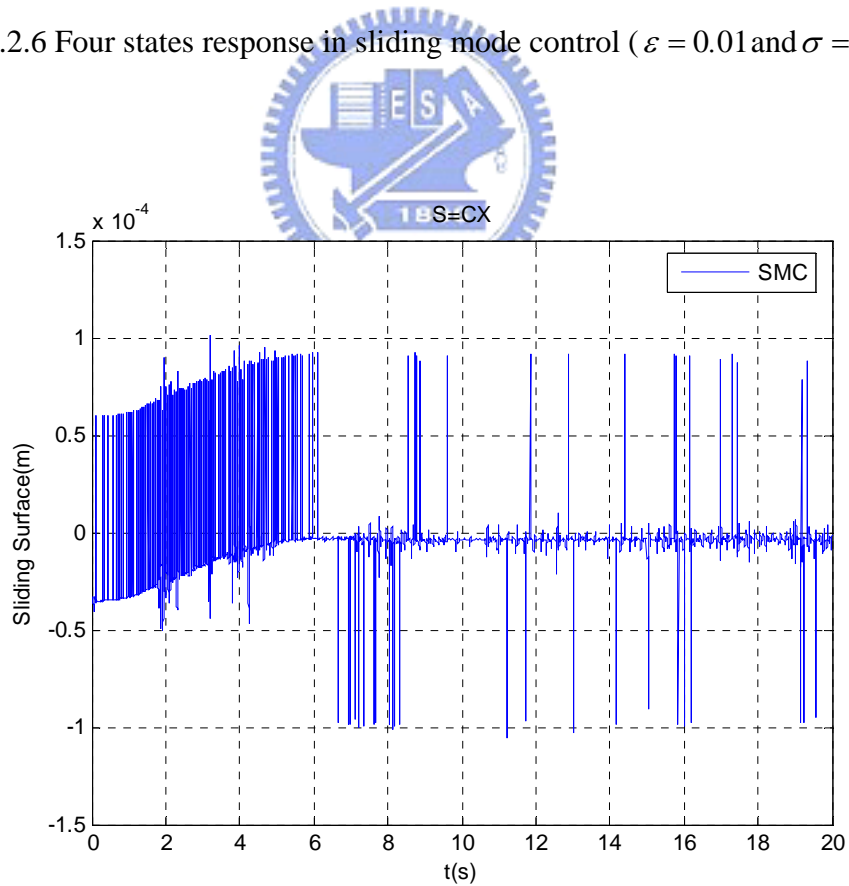


Fig. 5.2.7 Sliding surface in sliding mode control ( $\varepsilon = 0.01$  and  $\sigma = 5$ )

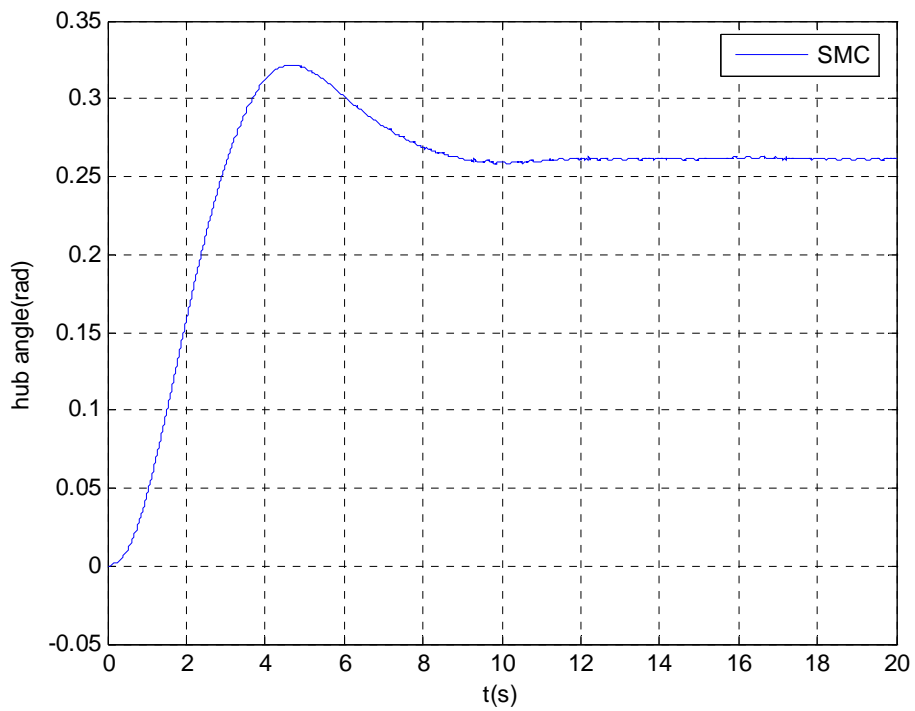


Fig. 5.2.8 Hub angle regulation in sliding mode control ( $\varepsilon = 0.0067$  and  $\sigma = 6$ )

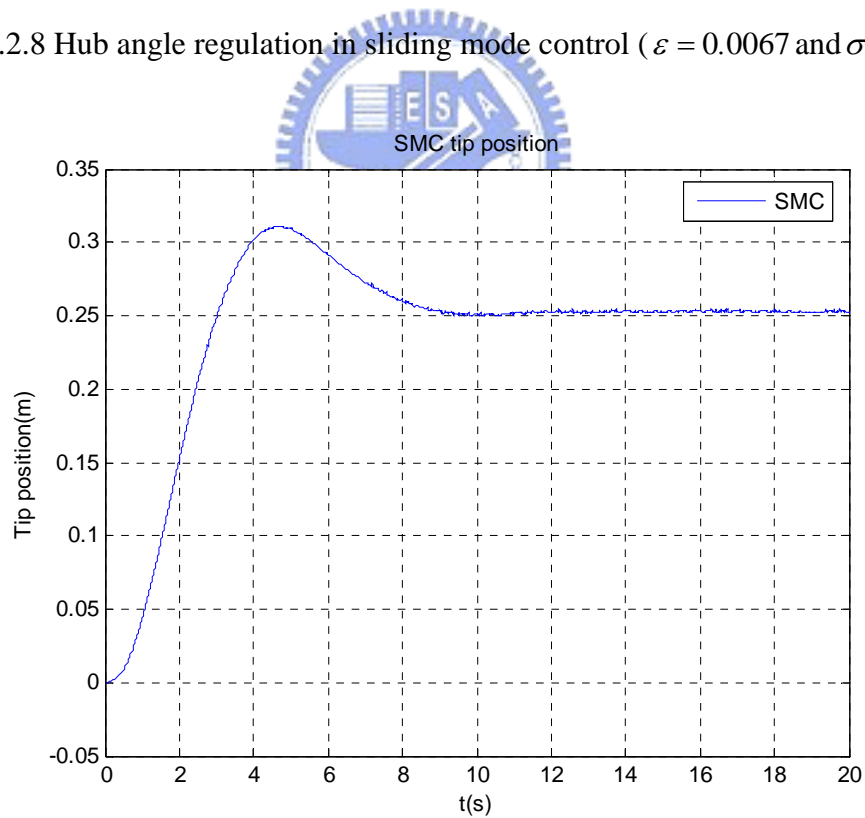


Fig. 5.2.9 Tip position regulation in sliding mode control ( $\varepsilon = 0.0067$  and  $\sigma = 6$ )

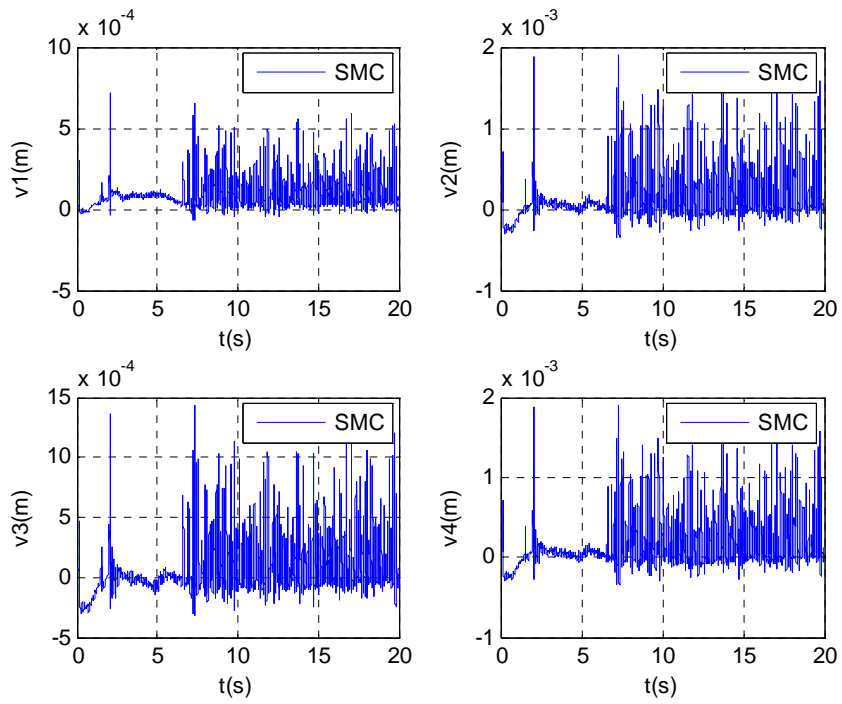


Fig. 5.2.10 Four states response in sliding mode control ( $\varepsilon = 0.0067$  and  $\sigma = 6$ )

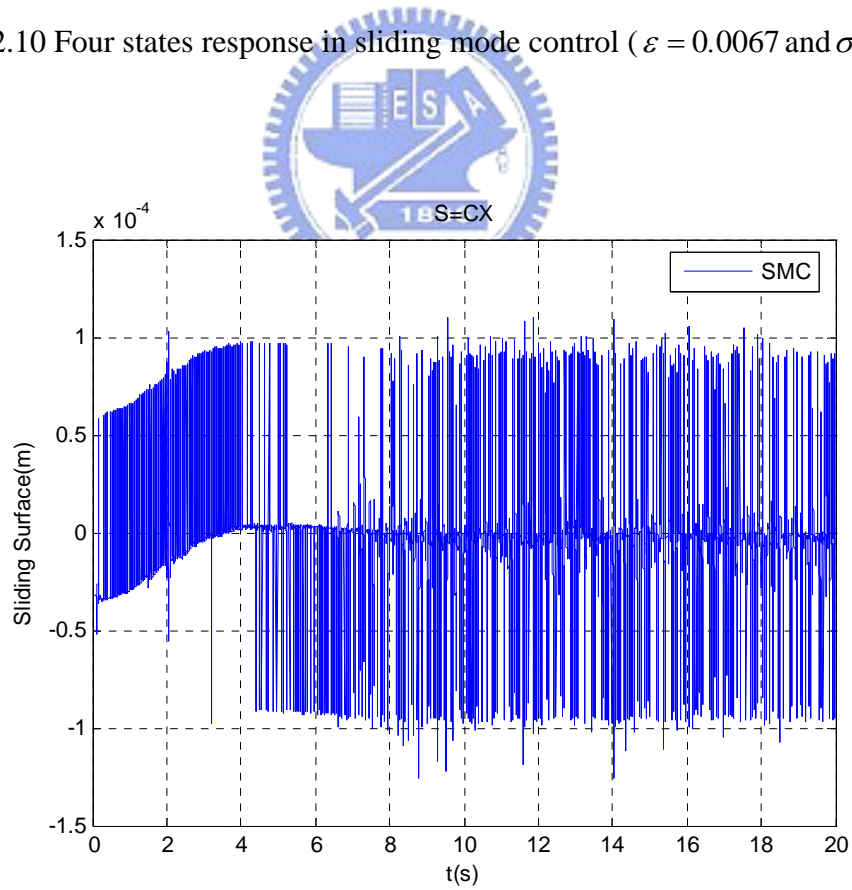


Fig. 5.2.11 Sliding surface in sliding mode control ( $\varepsilon = 0.0067$  and  $\sigma = 6$ )

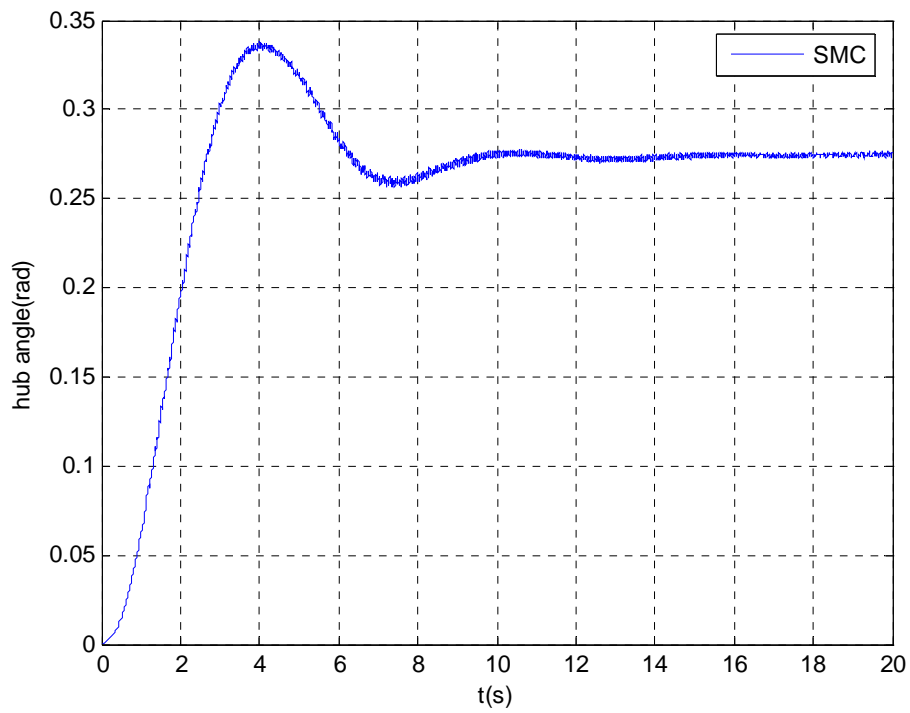


Fig. 5.2.12 Hub angle regulation in sliding mode control ( $\varepsilon = 0.005$  and  $\sigma = 8$ )

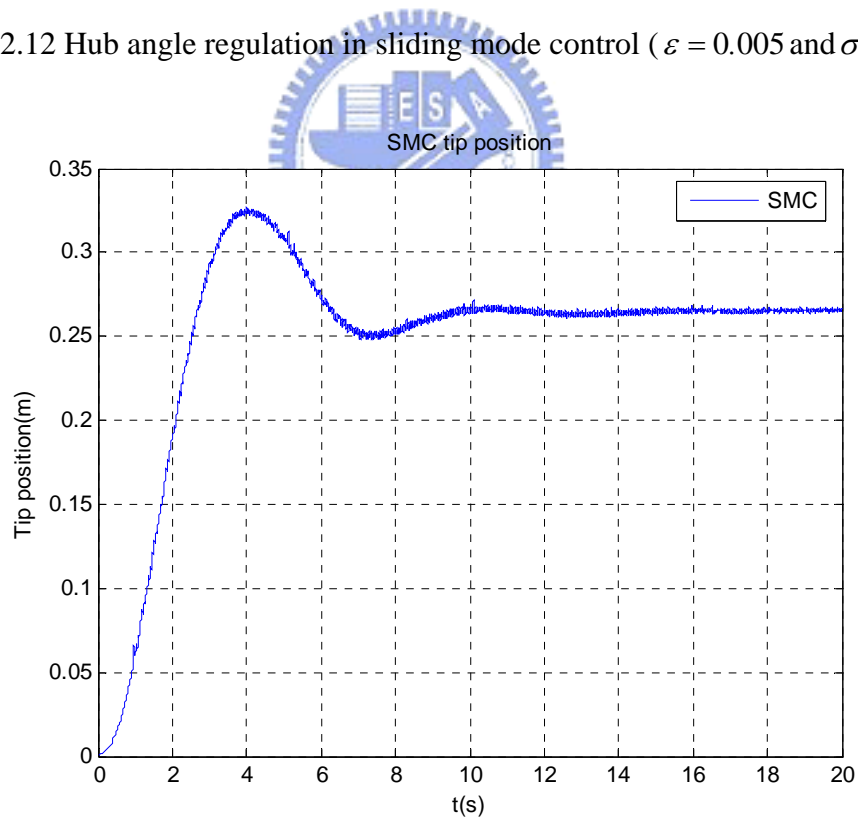


Fig. 5.2.13 Tip position regulation in sliding mode control ( $\varepsilon = 0.005$  and  $\sigma = 8$ )

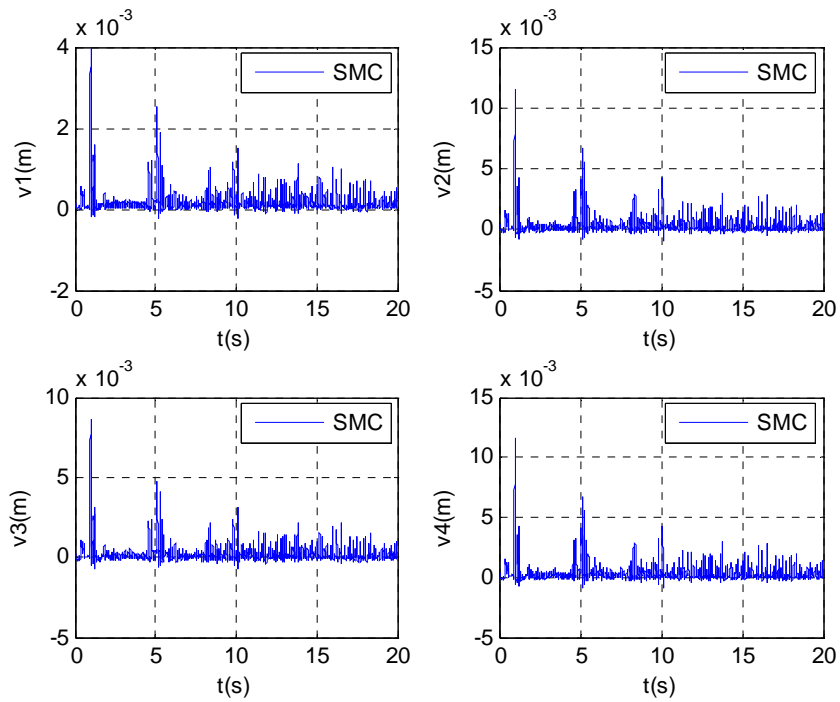


Fig. 5.2.14 Four states response in sliding mode control ( $\varepsilon = 0.005$  and  $\sigma = 8$ )

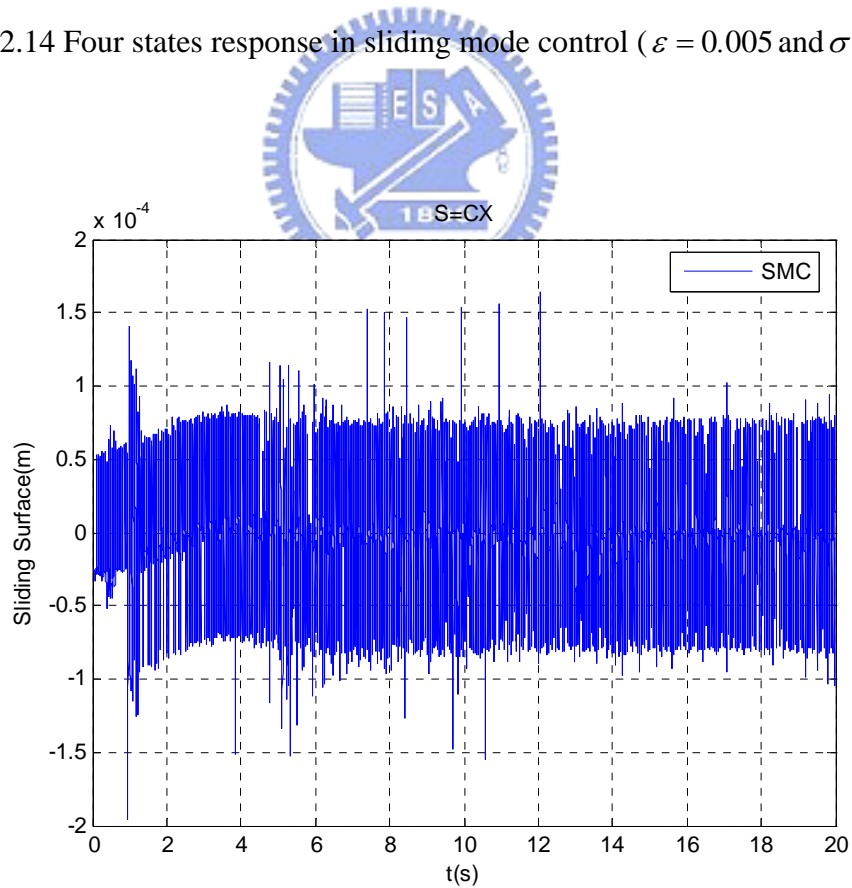
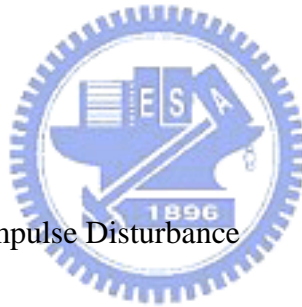


Fig. 5.2.15 Sliding surface in sliding mode control ( $\varepsilon = 0.005$  and  $\sigma = 8$ )

The experimental results obtained indicate sliding mode control is effectiveness in suppressing structural vibration of the flexible arm when regulating reference compared with the rigid controller. Simulation shows us that the experimental performance will be improved when we change the parameters  $\varepsilon$  and  $\sigma$  with proper values. But the experimental result is not well improved as we expected in the simulation. The error might come from the uncertainty of the system parameters, viscous hub friction, outer disturbance, and the error of the strain feedback. Among the uncertainties above, the error of the strain feedback seems to play the most important role.



### 5.3 Experimental Results of Impulse Disturbance

A robust system must be able to reject external impulse disturbance. To show such robustness of the proposed controller, an impulse disturbance which is taken as a knock to the root of the arm is applied when the controller is in use of a zero hub degree regulation. Two poles of a rigid controller are designed to  $-0.5$  and  $-2$ , and an impulse disturbance is applied about 3 seconds after the experiment is processing. The results for the hub angle and tip position which are presented in Fig 5.3.1 and 5.3.2 are vibrating to divergent. The states of FEM model are shown in Fig.5.3.3. The



frequency response of the hub angle is obtained by performing FFT to angle vibration from 11 seconds to 12 seconds in Fig.5.3.1, and the result is shown in Fig. 5.3.4. The dominant frequencies of the model derived in chapter 3 are excited for high response.

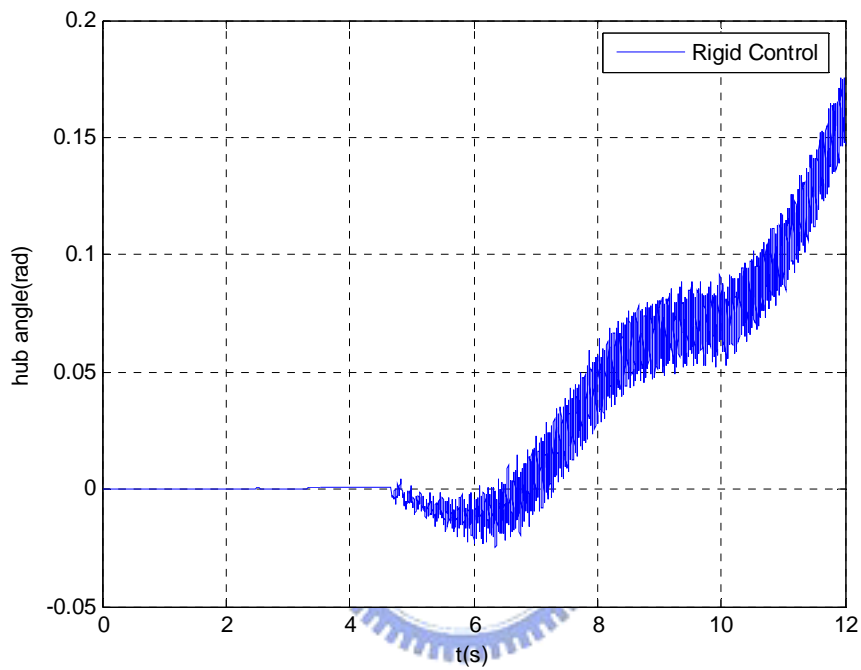


Fig. 5.3.1 Hub angle response in rigid control

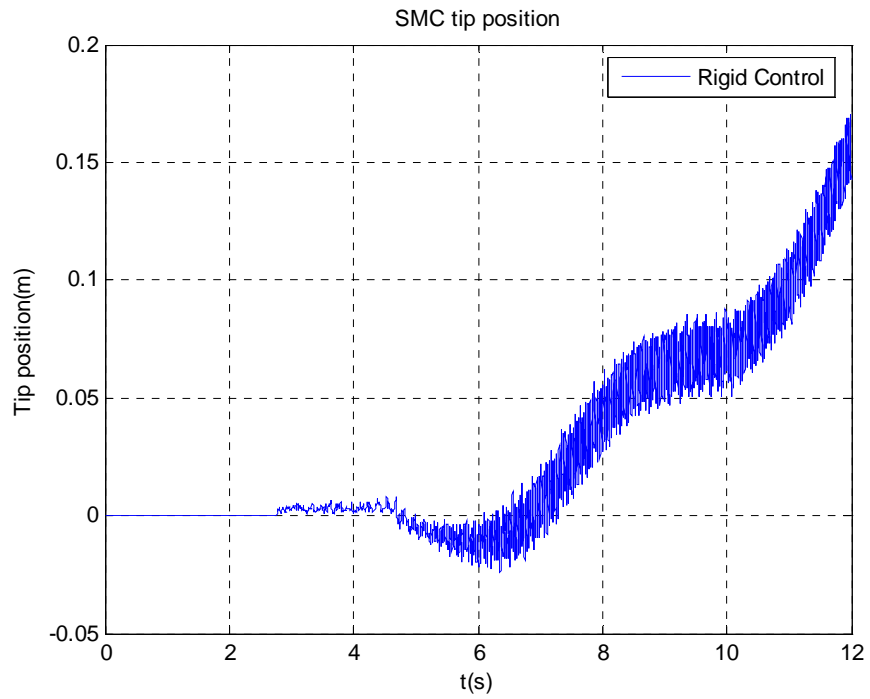


Fig. 5.3.2 Tip position response in rigid control

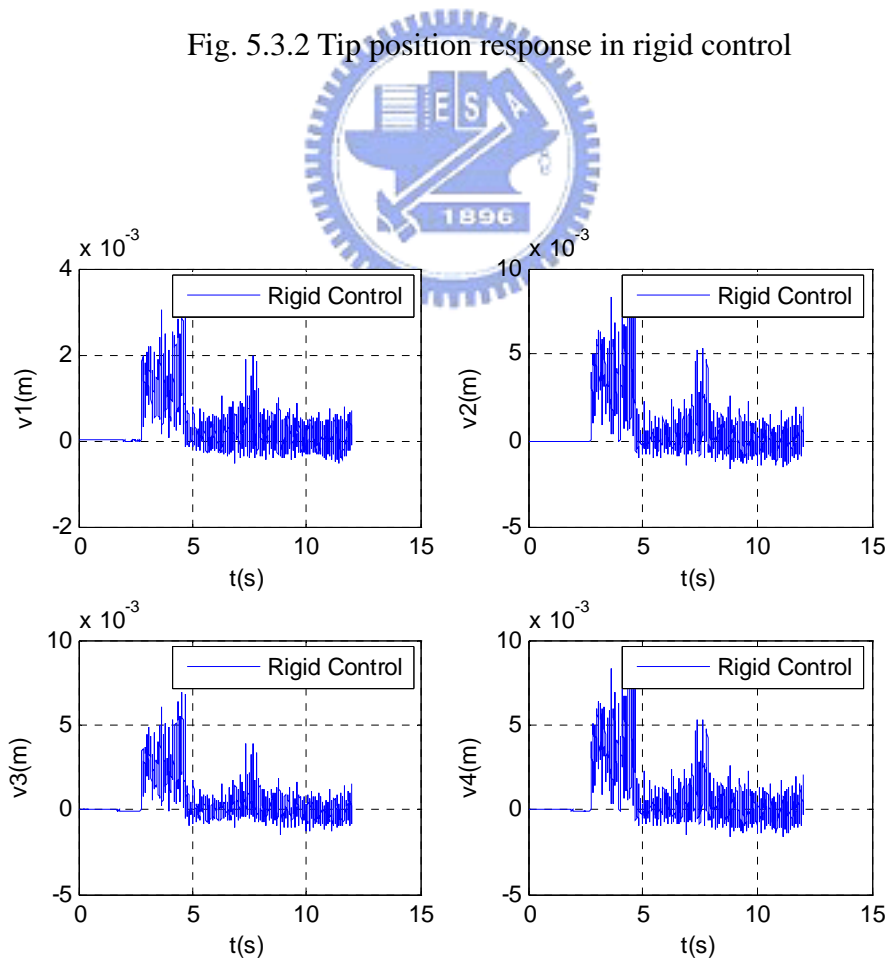


Fig. 5.3.3 Four states response in rigid control

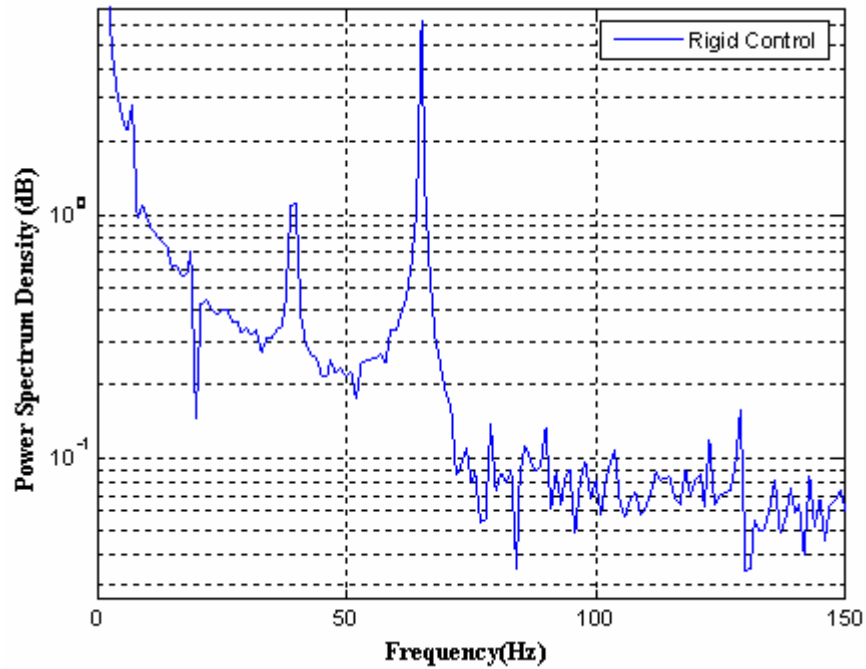


Fig. 5.3.4 Frequency response of vibration in rigid control

Then, in order to check the robustness of the sliding mode controller, the same impulse disturbance is applied when the sliding mode controller is in use of zero hub degree regulation about 3 seconds after the experiment is processing. The poles of the sliding mode controller are designed in the same position as in simulation. The results for the hub angle and tip position are presented in Fig 5.3.5, and 5.3.6. The states of FEM model and the sliding surface are shown in Fig. 5.3.7, and Fig. 5.3.8. The frequency response of the hub angle is obtained by performing FFT to the angle vibration from 17 seconds to 18 seconds in Fig. 5.3.5, and the result is shown in Fig. 5.3.9.

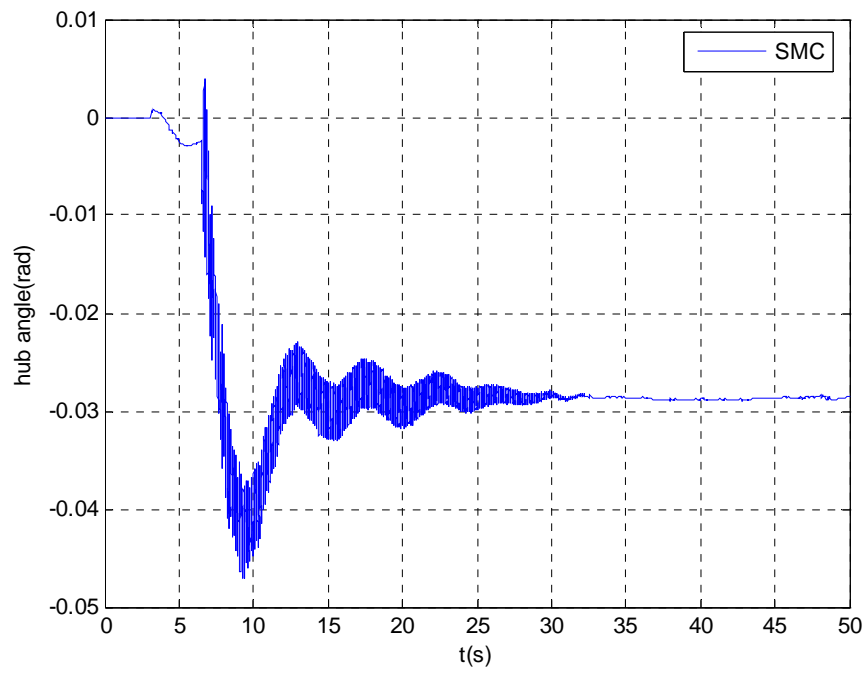


Fig. 5.3.5 Hub angle response in sliding mode control ( $\varepsilon = 0.01$  and  $\sigma = 5$ )

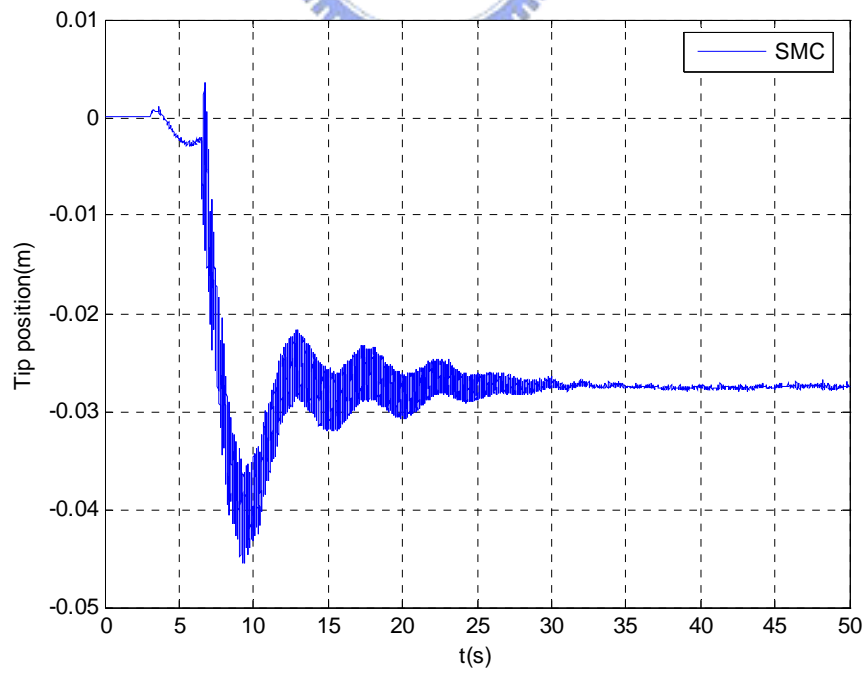
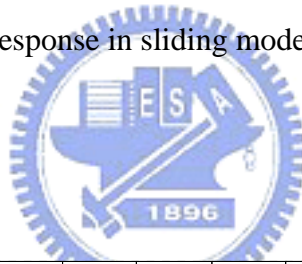


Fig. 5.3.6 Tip position response in sliding mode control ( $\varepsilon = 0.01$  and  $\sigma = 5$ )

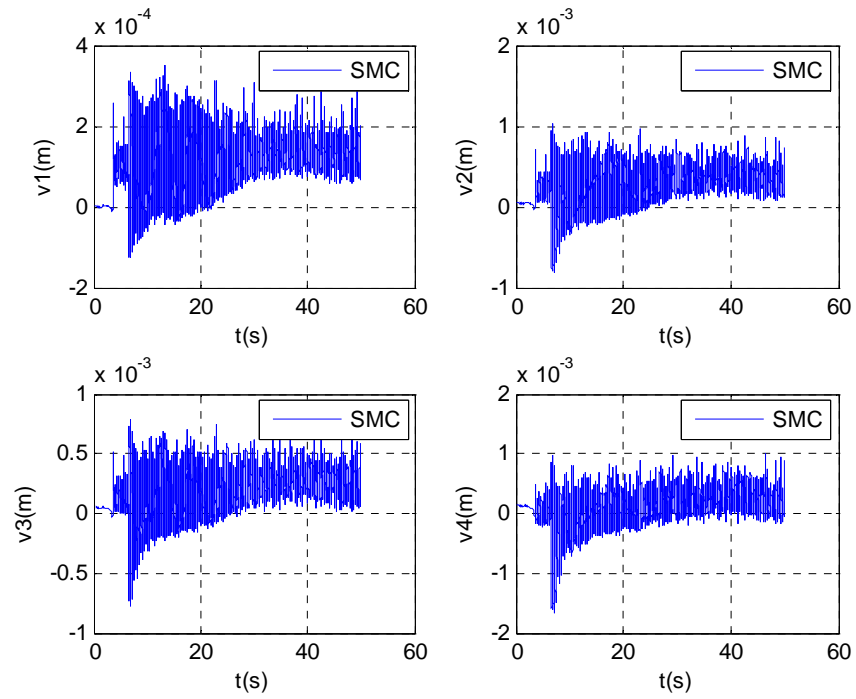


Fig. 5.3.7 Four states response in sliding mode control ( $\varepsilon = 0.01$  and  $\sigma = 5$ )

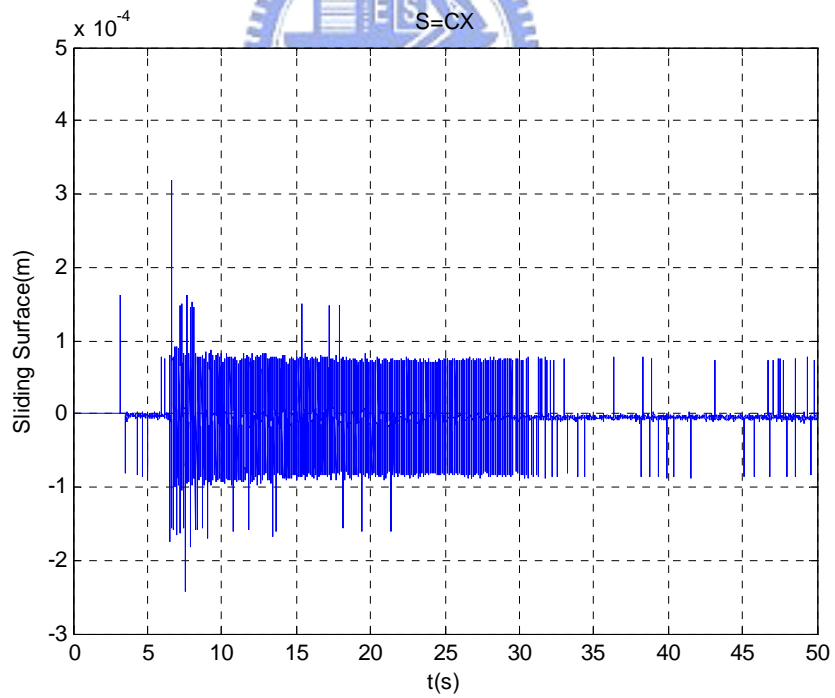


Fig. 5.3.8 Sliding surface in sliding mode control ( $\varepsilon = 0.01$  and  $\sigma = 5$ )

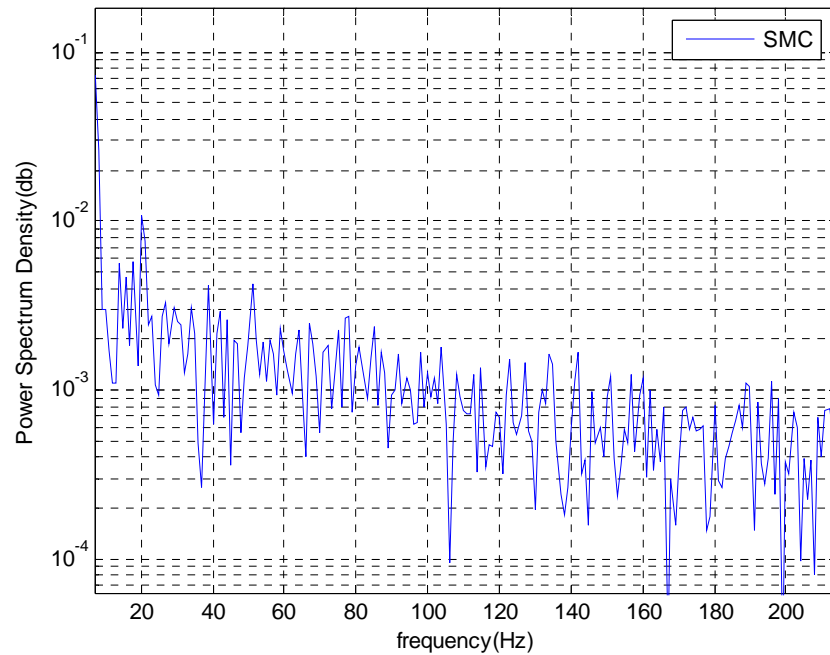
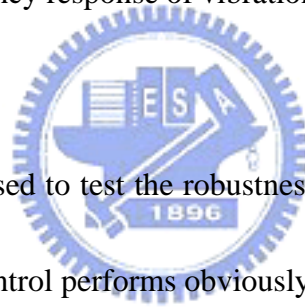


Fig. 5.3.9 Frequency response of vibration in sliding mode control



Impulse disturbance is used to test the robustness of the system. Compared with rigid control, sliding mode control performs obviously better. Vibration suppression in sliding mode control shown in Fig.5.3.4 is  $10^{-2}$  attenuate than the rigid control shown in Fig.5.3.9.

#### 5.4 Experimental Results with Tip-Mass Loading

The payload is considered as the system disturbance in these demonstrations. The experimental results of rigid controller whose poles designed in -0.5 and -2 for regulation problem are shown in Fig. 5.4.1 to Fig. 5.4.3., the tip position with 0.102

Kg payload reaches the reference goal with much vibration effect. Then, Fig.5.4.4 to Fig. 5.4.7 (Fig.5.4.8 to Fig. 5.4.11) show the robustness of the sliding mode control against 0.102 Kg payload variation with sliding layer parameters  $\varepsilon = 0.01$  and  $\sigma = 6$  ( $\varepsilon = 0.005$  and  $\sigma = 7$ ). The vibration phenomenon is suppressed in the process of regulation. The performance of sliding mode control is alike the non-payload ones but exist greater steady state errors.

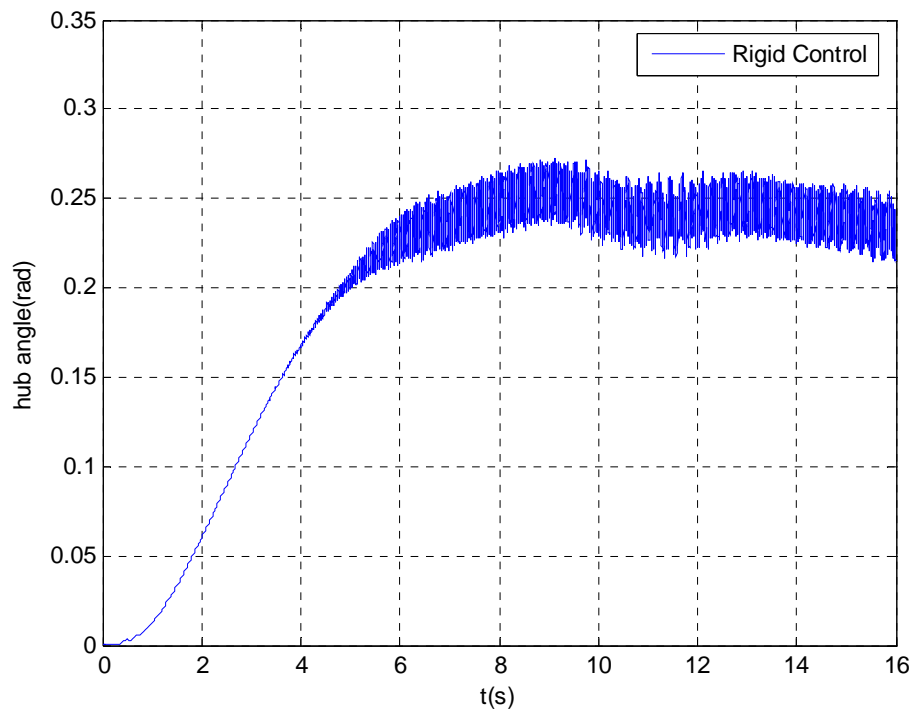


Fig. 5.4.1 Hub angle regulation in rigid control ( $m_t = 0.102$ kg)

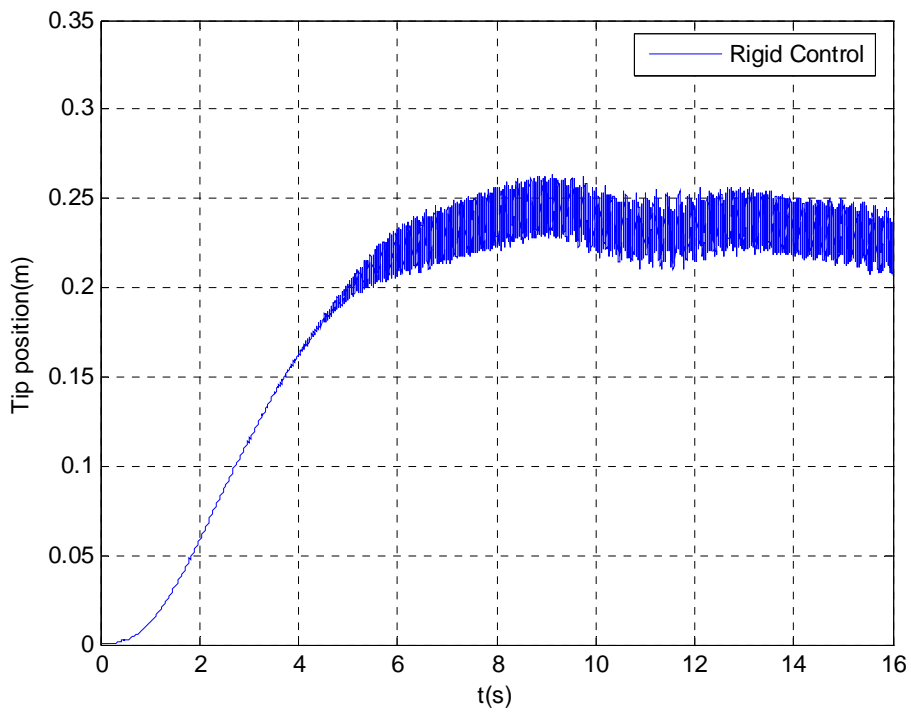


Fig. 5.4.2 Tip position regulation in rigid control ( $m_t = 0.102\text{ kg}$ )

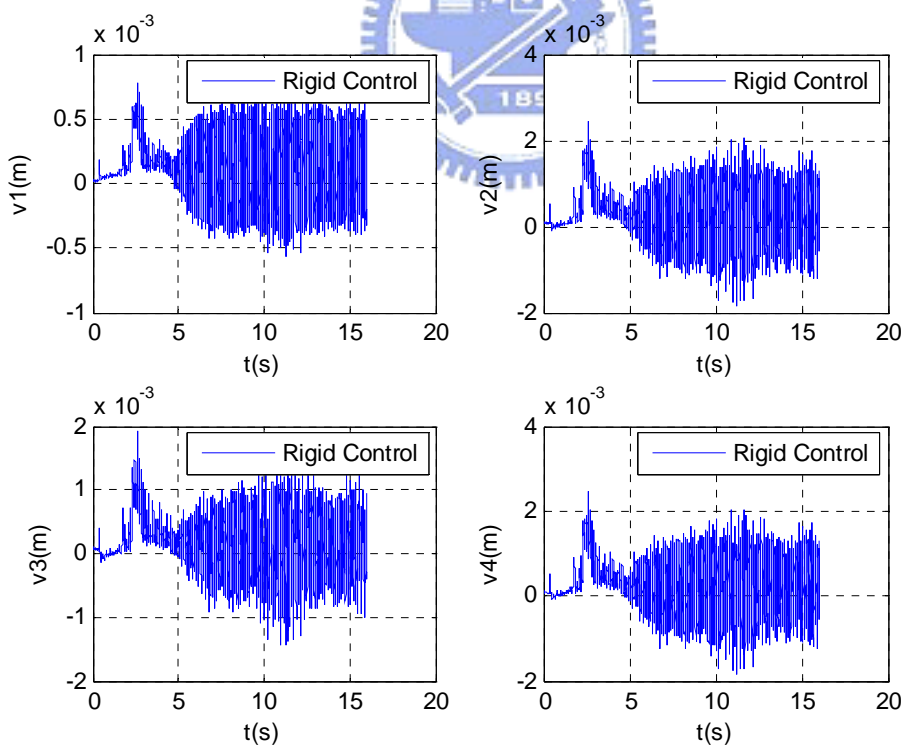


Fig. 5.4.3 Four states response in rigid control ( $m_t = 0.102\text{ kg}$ )



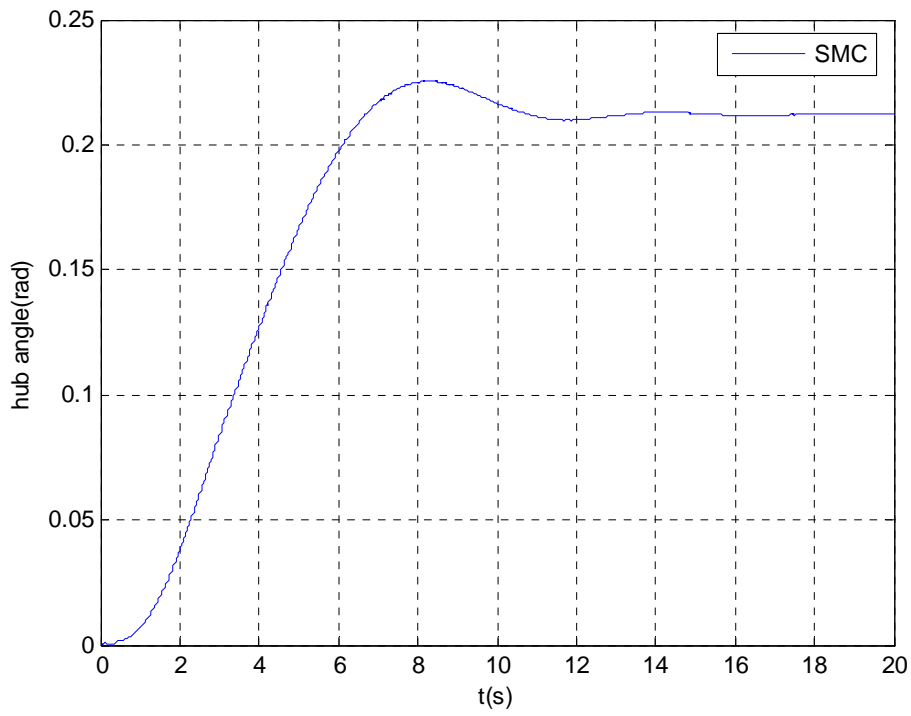


Fig. 5.4.4 Hub angle regulation in SMC ( $m_t = 0.102$  kg,  $\varepsilon = 0.01$  and  $\sigma = 6$ )

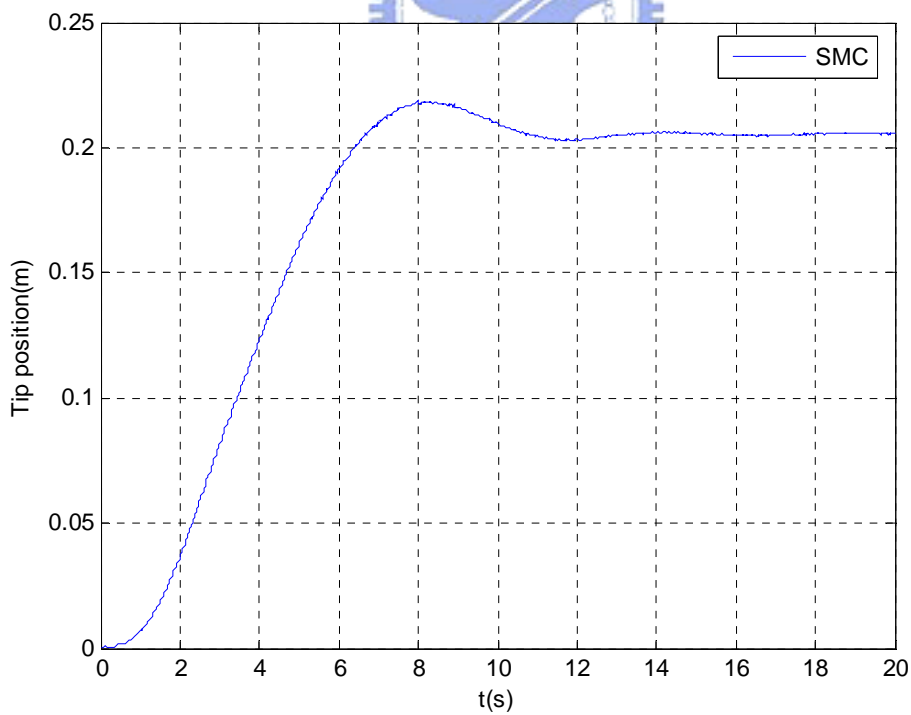


Fig. 5.4.5 Tip position regulation in SMC ( $m_t = 0.102$  kg,  $\varepsilon = 0.01$  and  $\sigma = 6$ )

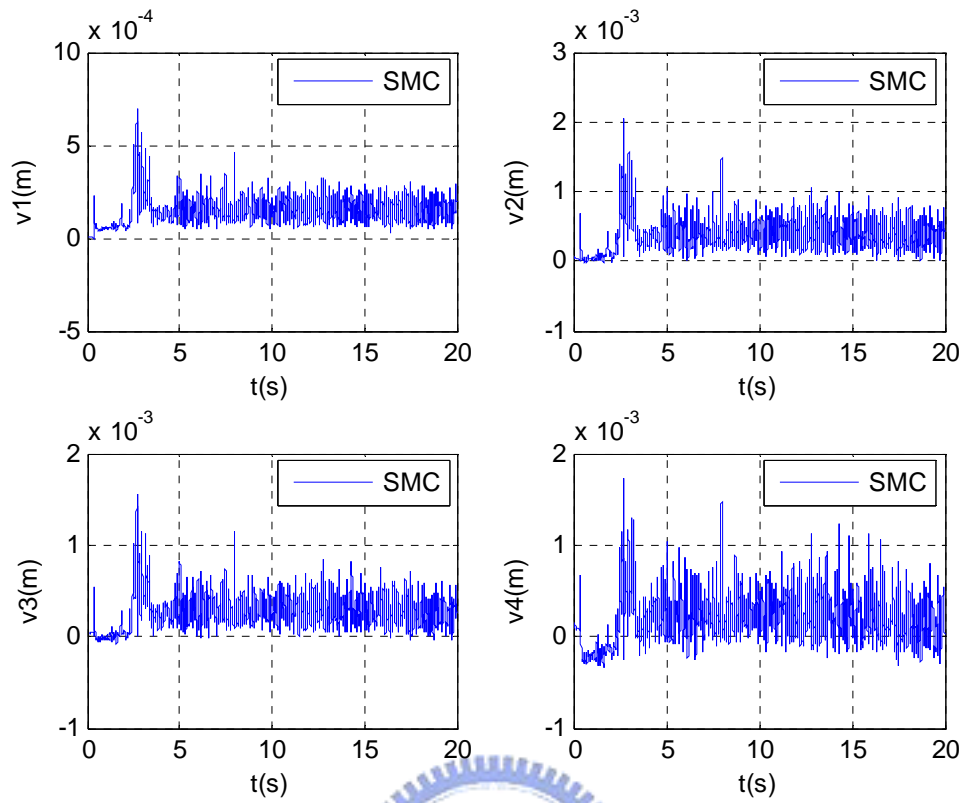


Fig. 5.4.6 Four states response in SMC ( $m_t = 0.102$  kg,  $\varepsilon = 0.01$  and  $\sigma = 6$ )

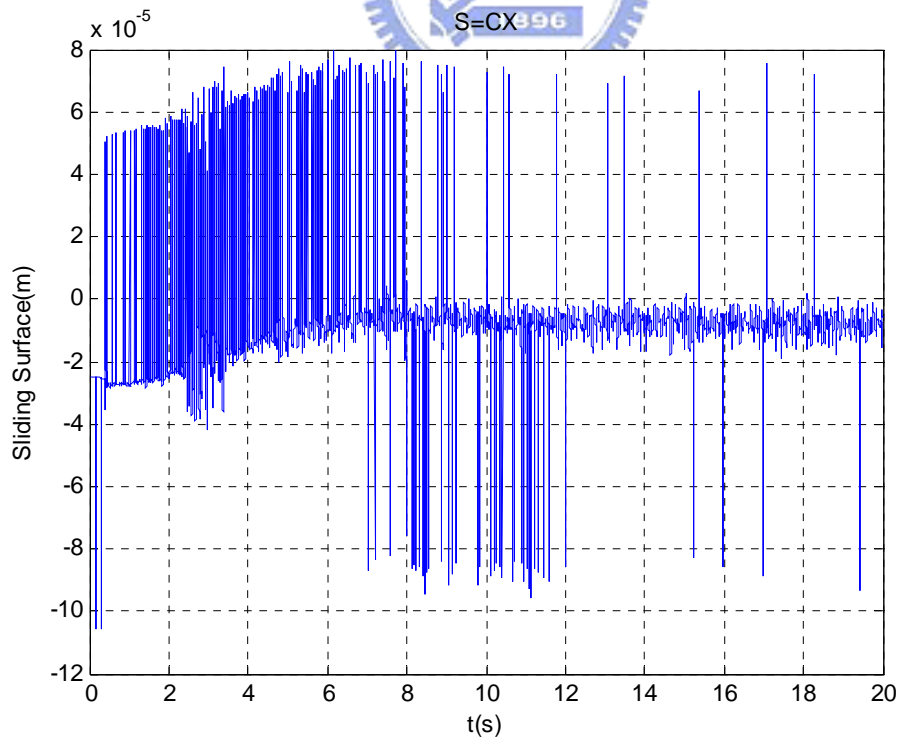


Fig. 5.4.7 Sliding surface in SMC ( $m_t = 0.102$  kg,  $\varepsilon = 0.01$  and  $\sigma = 6$ )

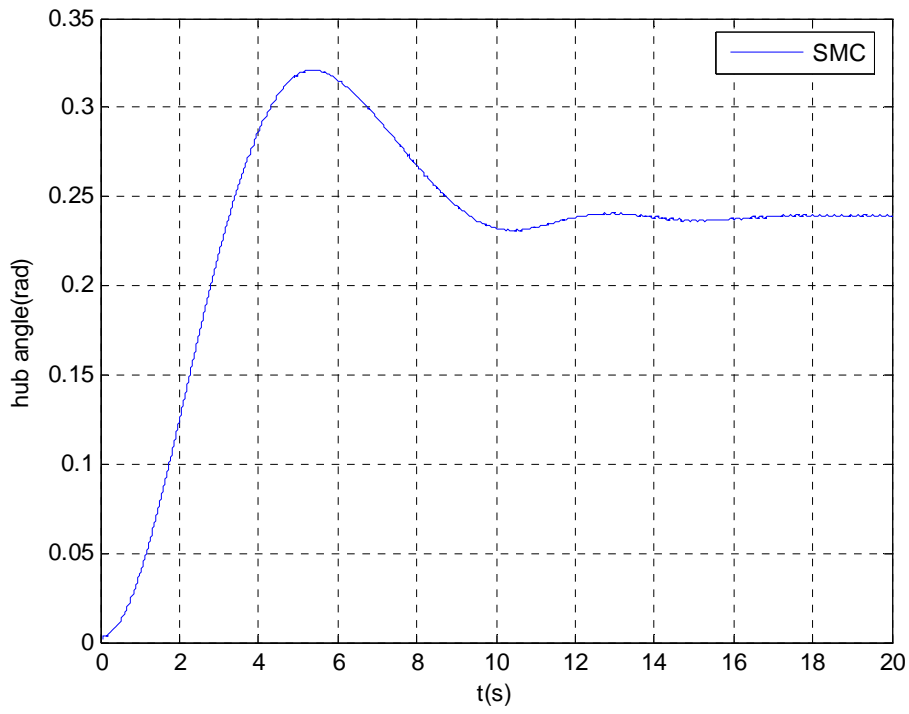


Fig. 5.4.8 Hub angle regulation in SMC ( $m_t = 0.102$  kg,  $\varepsilon = 0.005$  and  $\sigma = 7$ )

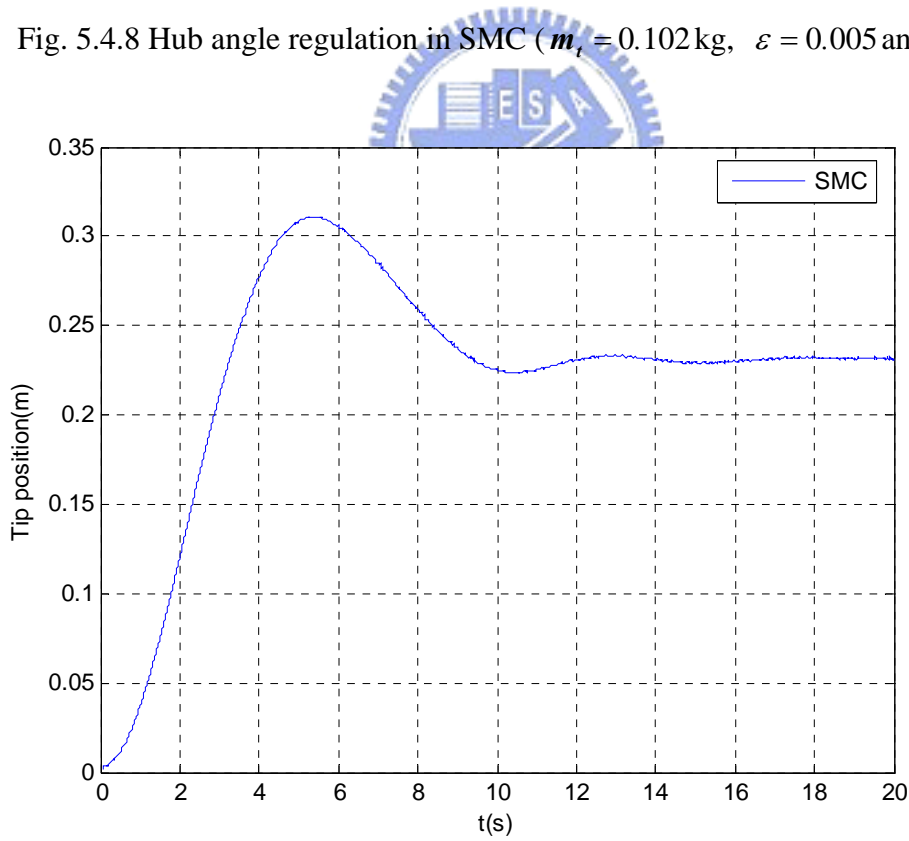


Fig. 5.4.5 Tip position regulation in SMC ( $m_t = 0.102$  kg,  $\varepsilon = 0.005$  and  $\sigma = 7$ )

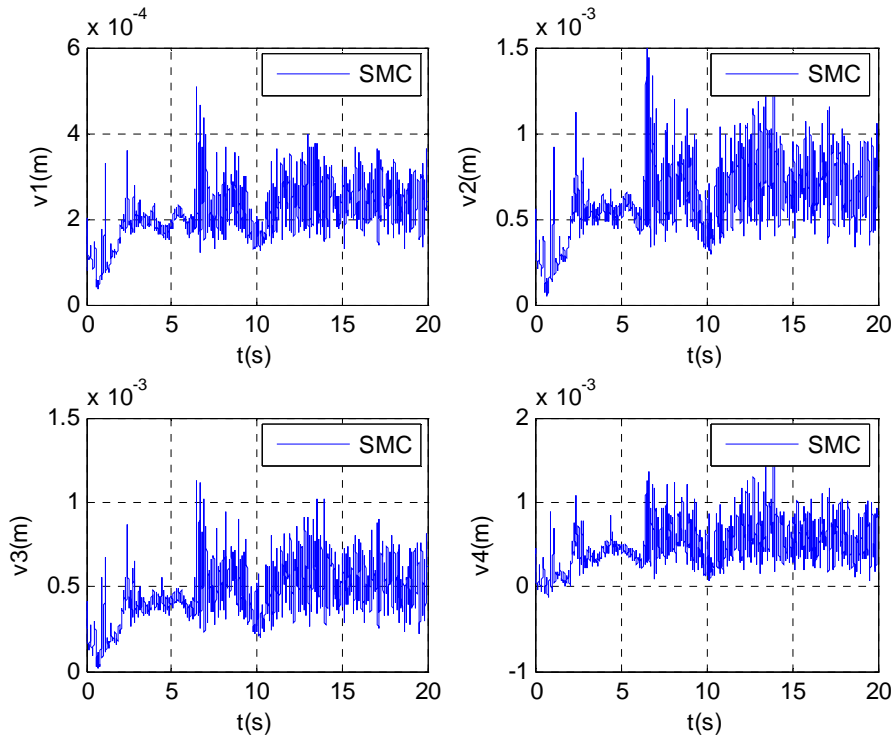


Fig. 5.4.6 Four states response in SMC ( $m_t = 0.102$  kg,  $\varepsilon = 0.005$  and  $\sigma = 7$ )

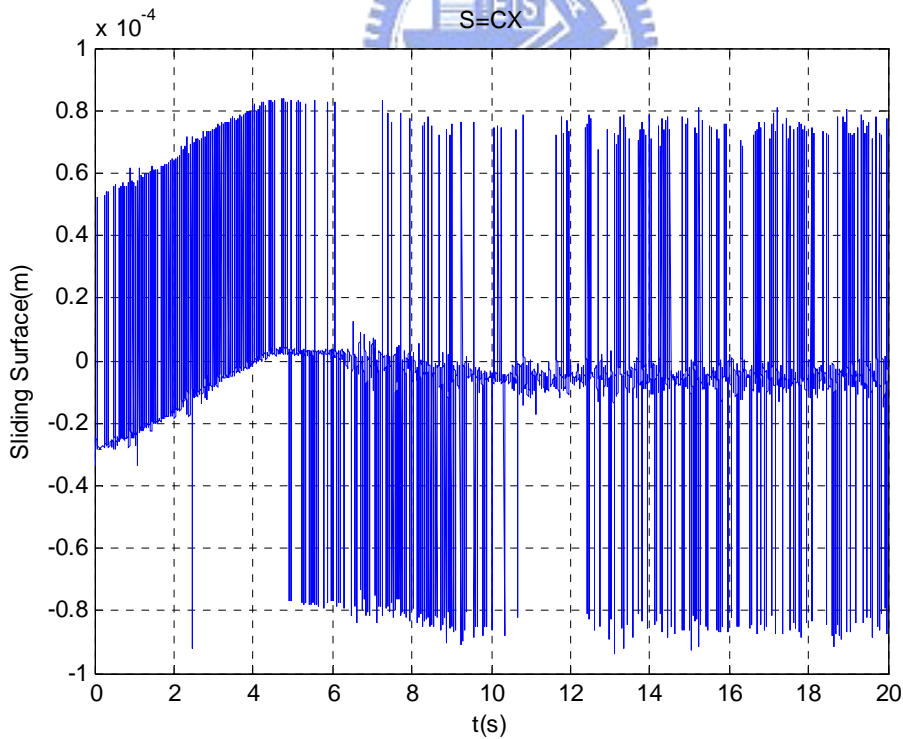


Fig. 5.4.7 Sliding surface in SMC ( $m_t = 0.102$  kg,  $\varepsilon = 0.005$  and  $\sigma = 7$ )

The results of sliding mode controller compared with rigid controller obviously indicated the robustness of sliding-mode controller against the variation of payload in these demonstrations.



# Chapter 6

## Conclusions

A physical sliding mode control is investigated in this thesis to deal with the vibration problem of the tip position control of a single-link flexible arm. Based on the linear model derived by the FEM method, the disturbances related to the higher order modes of the flexible arm and the uncertainties resulted from the structure and payload variations can be successfully suppressed by the sliding mode control with sliding surface designed by Lyapunov method. The simulation and experimental results demonstrate that the sliding mode controller not only requires small control torque but also highly reduces the vibration. Besides, the robustness of the flexible arm controlled by sliding mode method is also verified by applying an impulse disturbance and tip-mass variation. Because the real system may be not enough to be described by the 2-element FEM Euler-Bernoulli beam, in the future the system model might be derived by a more complicated analytic approach. For the better control result in our future work, the experimental accuracy should be improved by reducing the errors from the voltage shifting effect in strain gauges feedback.

## Reference

- [1] B. V. Chapnik, G. R. Heppler, and J. D. Aplevich, "Modeling Impact on a One-Link Flexible Robotic Arm," IEEE trans. on Robotics and automation, Vol. 7, No. 4, August 1991.
- [2] Y. P. Chen and H.T. Hsu, "Regulation and Vibration Control of an FEM-Based Single-Link Flexible Arm Using Sliding-Mode Theory," Journal of Vibration and Control, pp. 741-752, 2001.
- [3] R. A. Decarlo, S. H. Xak, and F. C. K. Cheung, "An approach of variable structure control of nonlinear multivariable systems: A tutorial," Proc. IEEE, vol. 76, pp. 212-232, Mar. 1988.
- [4] A. Garcia and V. Feliu, "Force Control of a Single-Link Flexible Robot Based on a collision detection mechanism," IEE Proc. Control Theory Appl., Vol. 147, No. 6, Nov., 2000.
- [5] G. G. Hastings and Wayne J. Book, "A Linear Dynamic Model for Flexible Robotic Manipulators," IEEE trans. on Control Systems, Feb. 1987.
- [6] M. Leonard, "Elements of Vibration Analysis," McGraw Hill, pp. 300-307, 1986.
- [7] M. L. James, "Vibration of Mechanical and Structural Systems: with Microcomputer Applications," Harper & Row, 1993.
- [8] J. F. Jansen, "Control and Analysis of a Single-Link Flexible Beam with Experimental Verification," Oak Ridge National Laboratory, Dec. 1992.
- [9] J. L. Junkins and Y. Kim, "Introduction to Dynamics and Control of Flexible Structures," AIAA, pp. 199-219, 1993.
- [10] Z. H. Luo, "Direct Strain Feedback Control of Flexible Robot Arms: New Theoretical and Experimental Results," IEEE trans. on Automatic Control, Vol.

38, No. 11, Nov., 1993.

- [11] W. T. Thomson and M. D. Dahleh, "Theory of Vibration with Applications 5<sup>th</sup> edition," Prentice Hall, pp. 292-295, 1998.
- [12] M. O. Tokhi, Z. Mohamed, S. G. M. Amin, and R. Mamat, "Dynamic Characterisation of a Flexible Manipulator System: Theory and Experiments," IEEE. 2000.
- [13] R. L. Wells, J. K. Schueller, and J. Tlustý, "Feedforward and Feedback Control of a Flexible Robotic Arm," IEEE trans. on Control Systems, Jan. 1990.
- [14] H. Yang, J. Hong, and Z. Yu, "Dynamic modeling of a flexible hub-beam system with a tip mass," Journal of Sound and Vibration 266, pp. 759-774, 2003.
- [15] 陳永平，張俊林，"可變結構控制設計"，全華科技圖書股份有限公司，2002.
- [16] 張俊林，"單軸饒性手臂定力控制"，國立交通大學控制工程研究所碩士論文，1994.
- [17] 許懷德，"Modified Sliding Mode Control Applied to FEM-based Single Flexible Arm,"，國立交通大學控制工程研究所碩士論文，1997.
- [18] 林建宏，"Sliding Mode Control Applied to Single Flexible Arm,"，國立交通大學控制工程研究所碩士論文，1995.
- [19] 蔡永智，"The Motion Control of Flexible Beam Structure"，逢甲大學自動控制工程研究所碩士論文，1998.
- [20] Mitsubishi，MR-J2S-A，伺服驅動器技術資料集.



# Appendix A

## Local Mass Matrix and Stiffness Matrix

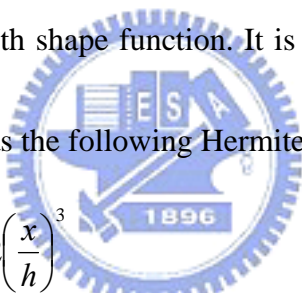
For the Euler-Bernoulli beam introduced in Chapter 2, its local mass matrix in (2.2.9) and stiffness matrix in (2.2.8) are respectively given as

$$[\mathbf{M}^i]_{jk} = \int_0^h \rho \phi_j(x) \phi_k(x) dx \quad (\text{A.1})$$

and

$$[\mathbf{K}^i]_{jk} = \int_0^h EI \phi_j''(x) \phi_k''(x) dx \quad (\text{A.2})$$

where  $\phi_j(x)$  represents the  $j$ -th shape function. It is known that the shape functions are admissible and expressed as the following Hermite-cubic polynomial functions:


$$\begin{aligned} \phi_1(x) &= 1 - 3\left(\frac{x}{h}\right)^2 + 2\left(\frac{x}{h}\right)^3 \\ \phi_2(x) &= x - 2h\left(\frac{x}{h}\right)^2 + h\left(\frac{x}{h}\right)^3 \\ \phi_3(x) &= 3\left(\frac{x}{h}\right)^2 - 2\left(\frac{x}{h}\right)^3 \\ \phi_4(x) &= -h\left(\frac{x}{h}\right)^2 + h\left(\frac{x}{h}\right)^3 \end{aligned} \quad (\text{A.3})$$

which as been shown in (2.2.14).

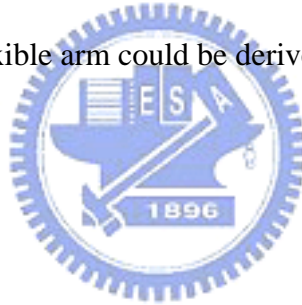
Finite element modeling of a structure may be considered to be many fold local application of the assumed modes method wherein linear combinations of the locally valid  $\phi_i(x)$ s are used to represent the deflection shape over a portion (finite element) of the structure, and with the element equations and boundary constraints being

assembled to form a global model of the structural system. For the general expressions of the Euler-Bernoulli beam elements. Substituting the four shape functions (A.3) into (A.1) and (A.2), the mass matrix  $\mathbf{M}^i$  and the stiffness matrix  $\mathbf{K}^i$  of the  $i$ -th element are obtained as

$$\mathbf{M}^i = \frac{\rho h}{420} \begin{bmatrix} 156 & 22h & 54 & -13h \\ 22h & 4h^2 & 13h & -3h^2 \\ 54 & 13h & 156 & -22h \\ -13h & -3h^2 & -22h & 4h^2 \end{bmatrix}$$

$$\mathbf{K}^i = \frac{EI}{h^3} \begin{bmatrix} 12 & 6h & -12 & 6h \\ 6h & 4h^2 & -6h & 2h^2 \\ -12 & -6h & 12 & -6h \\ 6h & 2h^2 & -6h & 4h^2 \end{bmatrix}$$

Then,  $N$ -element model of flexible arm could be derived with the above result.



## Appendix B

### Measurement of Young's Modulus

Young's modulus  $E$  is an important parameter for the precise flexible arm model, and it is measured by the frequencies analysis in this thesis. At first, the flexible arm dynamic equation is described as

$$\frac{\partial^2}{\partial x^2} \left( EI \frac{\partial^2 w}{\partial x^2} \right) + \rho \frac{\partial^2 w}{\partial t^2} = p \quad (\text{B.1})$$

where  $p$  is external force which is assumed to be zero. Then, let the deformation  $w$  represented as

$$w(x,t) = w(x) \cos(\omega t - \phi) \quad (\text{B.2})$$

Substituting (B.2) into (B.1) yields

$$\frac{\partial^2}{\partial x^2} \left( EI \frac{\partial^2 w}{\partial x^2} \right) + \rho \omega^2 w = 0 \quad (\text{B.3})$$

Because the flexible arm is uniform in shape and property, its area moment of inertia  $I$

and Young's modulus  $E$  are constant. Rewrite (B.3) as

$$\frac{d^4 w}{dx^4} + \lambda^4 w = 0 \quad (\text{B.3})$$

where  $\lambda^4 = \frac{(\rho \omega^2)}{EI}$  (B.4)

The general solution of (B.4) is

$$w(x) = A_1 e^{\lambda x} + A_2 e^{-\lambda x} + A_3 e^{i\lambda x} + A_4 e^{-i\lambda x} \quad (\text{B.5})$$

or

$$w(x) = C_1 \sinh \lambda x + C_2 \cosh \lambda x + C_3 \sin \lambda x + C_4 \cos \lambda x \quad (\text{B.6})$$

The boundary conditions at the clamped end,  $x=0$ , are

$$w(0) = 0, \quad \left. \frac{dw}{dx} \right|_{x=0} = 0 \quad (\text{B.7})$$

On the other hand, at the free end,  $x=l$ , the boundary conditions are

$$\left. \frac{d^2 w}{dx^2} \right|_{x=l} = 0, \quad \left. \frac{d^3 w}{dx^3} \right|_{x=l} = 0 \quad (\text{B.8})$$

Evaluating the boundary conditions at  $x=0$  and  $x=l$  leads to the following homogeneous system of algebraic equations

$$\begin{bmatrix} 0 & 1 & 0 & 1 \\ \lambda & 0 & \lambda & 0 \\ \lambda^2 \sinh \lambda l & \lambda^2 \cosh \lambda l & -\lambda^2 \sin \lambda l & -\lambda^2 \cos \lambda l \\ \lambda^3 \cosh \lambda l & \lambda^3 \sinh \lambda l & -\lambda^3 \cos \lambda l & \lambda^3 \sin \lambda l \end{bmatrix} \begin{bmatrix} C_1 \\ C_2 \\ C_3 \\ C_4 \end{bmatrix} = \begin{bmatrix} 0 \\ 0 \\ 0 \\ 0 \end{bmatrix} \quad (\text{B.9})$$

For the set of homogeneous equations to have a nontrivial solution, the determinant of the coefficients must vanish. It follows that the determinant vanishes if and only if  $\lambda$  is such that the following condition holds

$$\cos \lambda l \cosh \lambda l + 1 = 0 \quad (\text{B.10})$$

which is recognized as the characteristic equation. The explicit expression for the roots of this characteristic equation is not simple, so these roots must be determined using some numerical method, generally yielding an infinite set of eigenvalues  $\lambda_r (r=1,2,\dots)$ . The first few eigenvalues are given approximately as

follows

$$\lambda_1 l = 1.8751 \quad \lambda_2 l = 4.6941 \quad \lambda_3 l = 7.8548 \quad (\text{B.11})$$

From (B.4)

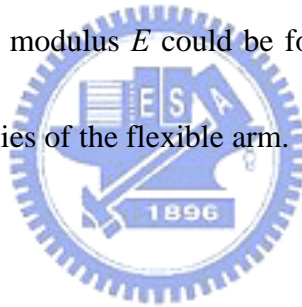
$$w_r = \frac{(\lambda_r l)^2}{l^2} \left( \frac{EI}{\rho} \right)^{\frac{1}{2}} \quad (r = 1, 2, \dots) \quad (\text{B.12})$$

Therefore, the approximate values of the first three natural frequencies are obtained as

follows

$$w_1 = \frac{3.516}{l^2} \left( \frac{EI}{\rho} \right)^{\frac{1}{2}} \quad w_2 = \frac{22.03}{l^2} \left( \frac{EI}{\rho} \right)^{\frac{1}{2}} \quad w_3 = \frac{61.70}{l^2} \left( \frac{EI}{\rho} \right)^{\frac{1}{2}} \quad (\text{B.13})$$

Based on (B.13), the Young's modulus  $E$  could be found by getting the first several order resonant nature frequencies of the flexible arm.



## Appendix C

### Design Sliding Surface by Lyapunov Method

There are several methods to design the sliding surface. The Lyapunov method which is developed from the aspect of the energy convergence is the easiest one inside them. Assume the original system is

$$\dot{\mathbf{x}} = \mathbf{A}\mathbf{x} + \mathbf{B}\mathbf{u} + \mathbf{d} \quad (\text{C.1})$$

where  $\mathbf{d}$  is disturbance. In order to use Lyapunov method, by pole placement method the feedback matrix  $\mathbf{K}$  should be obtained first so that all the eigenvalues of the matrix

$$\mathbf{A}_s = \mathbf{A} - \mathbf{B}\mathbf{K} \quad (\text{C.2})$$

are lied in the left half plane of  $s$  domain. Then, the input is designed as

$$\mathbf{u} = -\mathbf{K}\mathbf{x} + \mathbf{v} \quad (\text{C.3})$$

(C.1) is rearranged as

$$\dot{\mathbf{x}} = \mathbf{A}_s\mathbf{x} + \mathbf{B}\mathbf{v} + \mathbf{B}\mathbf{d}_m + \mathbf{B}_r\mathbf{d}_r \quad (\text{C.4})$$

where

$\mathbf{d}_m$  is matched disturbance

$\mathbf{d}_r$  is mismatched disturbance

$\mathbf{B}_r$  is the null space of matrix  $\mathbf{B}$

For every positive-definite matrix  $\mathbf{Q}$ , The positive-definite matrix  $\mathbf{P}$  is surely uniquely exist and satisfying the Lyapunov equation below.

$$A_s^T P + P A_s = -Q \quad (C.5)$$

According to (3.3.2.13), the P matrix is calculated and analyzed for the system stability, define

$$V(x) = x^T P x \quad (C.6)$$

Substituting (C.1) and (C.4) into (C.6) yields

$$\dot{V}(x) = -x^T Q x + 2x^T P B (v + d_m) + 2x^T P B_r d_r \quad (C.7)$$

In equation (C.7), if the mismatched disturbance is neglect and the condition  $B^T P x = 0$  is included, (C.7) is written as

$$\dot{V}(x) = -x^T Q x \leq 0 \quad (C.8)$$

The equal appears when x is equal to zero,  $V(x)$  is a Lyapunov function. The system is stable because that the infinity of x tends to become zero. If the mismatched disturbance  $d_r$  is neglected, the stable system occurs when the sliding surface was chosen as

$$s = Cx = B^T P x = 0 \quad (C.9)$$

In the same time, the control goal is accomplished.